Key Points:
- Dynamical response to MJO convection weakens in warmer climate, a result of increased static stability
- Weakened dynamical response to MJO convection reduces MJO's ability to influence the extratropics
- MJO convection drives stronger variations in vertical moisture advection in warmer climate, supporting destabilization of the MJO

Correspondence to:
B. O. Wolding,
brandon.wolding@gmail.com

Climate change and the Madden-Julian Oscillation: A vertically resolved weak temperature gradient analysis

Brandon O. Wolding[1] (iD)**, Eric D. Maloney[1]** (iD)**, Stephanie Henderson[1]** (iD)**, and Mark Branson[1]** (iD)

[1]Department of Atmospheric Science, Colorado State University, Fort Collins, Colorado, USA

Abstract WTG balance is used to examine how changes in the moist thermodynamic structure of the tropics affect the MJO in two simulations of the Superparameterized Community Earth System Model (SP-CESM), one at preindustrial (PI) levels of CO_2 and one where CO_2 levels have been quadrupled ($4\times CO_2$). While MJO convective variability increases considerably in the $4\times CO_2$ simulation, the dynamical response to this convective variability decreases. Increased MJO convective variability is shown to be a robust response to the steepening vertical moisture gradient, consistent with the findings of previous studies. The steepened vertical moisture gradient allows MJO convective heating to drive stronger variations in large-scale vertical moisture advection, supporting destabilization of the MJO. The decreased dynamical response to MJO convective variability is shown to be a consequence of increased static stability, which allows weaker variations in large-scale vertical velocity to produce sufficient adiabatic cooling to balance variations in MJO convective heating. This weakened dynamical response results in a considerable reduction of the MJO's ability to influence the extratropics, which is closely tied to the strength of its associated divergence. A composite lifecycle of the MJO was used to show that northern hemisphere extratropical 525 hPa geopotential height anomalies decreased by 27% in the $4\times CO_2$ simulation, despite a 22% increase in tropical convective heating associated with the MJO. Results of this study suggest that while MJO convective variability may increase in a warming climate, the MJO's role in "bridging weather and climate" in the extratropics may not.

1. Introduction

Two fundamental features of the tropics, the large Rossby radius of deformation and the strong influence of free tropospheric humidity on convection [*Bretherton et al.*, 2004; *Peters and Neelin*, 2006; *Neelin et al.*, 2009; *Sahany et al.*, 2012], help promote interactions between convection and large-scale circulations. Moisture mode theory [*Sobel et al.*, 2001; *Raymond*, 2001; *Fuchs and Raymond*, 2005; *Raymond and Fuchs*, 2009; *Sobel and Maloney*, 2012; *Arnold and Randall*, 2015; *Adames and Kim*, 2016] posits that such interactions play an important role in organizing the Madden-Julian Oscillation (MJO), an intraseasonal phenomena characterized by broad envelopes of enhanced and suppressed convection coupled to large-scale circulations that propagate slowly eastward from the Indian to west Pacific Oceans [*Madden and Julian*, 1971, 1972; *Zhang*, 2005]. The MJO dominates tropical variability on weekly to monthly timescales and has such a profound influence on tropical precipitation and wind that its signal can often be visually discerned in raw data [*Zhang*, 2005]. In addition to its direct impacts on tropical rainfall and winds, the MJO strongly modulates tropical cyclone activity in all basins [*Maloney and Hartmann*, 2000a, 2000b; *Hall et al.*, 2001; *Slade and Maloney*, 2013] and interacts with ENSO [*McPhaden*, 1999; *Takayabu et al.*, 1999].

The influence of the MJO extends well beyond the tropics. It has long been recognized that tropical convective variability has the ability to influence the extratropics [*Bjerknes*, 1966] by exciting stationary Rossby wave trains [*Hoskins and Karoly*, 1981; *Sardeshmukh and Hoskins*, 1988; *Hoskins and Ambrizzi*, 1993; *Jin and Hoskins*, 1995; *Trenberth et al.*, 1998], and the MJO is a well-documented example of this (see review in *Lau et al.* [2012]). Briefly, the MJO has been shown to influence extratropical modes of variability including the North Atlantic Oscillation (NAO) [*Cassou*, 2008; *Lin et al.*, 2009], Northern Annular Mode (NAM) [*Zhou and Miller*, 2005; *L'Heureux and Higgins*, 2008], Southern Annular Mode (SAM) [*Carvalho et al.*, 2005], and the Pacific-North-America Pattern (PNA) [*Mori and Watanabe*, 2008; *Johnson and Feldstein*, 2010], and significantly impact regional surface temperature in North America [*Vecchi and Bond*, 2004; *Zhou et al.*, 2012],

violent tornado outbreaks in North America [*Thompson and Roundy*, 2013], Northern Hemisphere winter blocking [*Hamill and Kiladis*, 2014; *Henderson et al.*, 2016], and atmospheric rivers impacting the west coast of North America [*Mundhenk et al.*, 2016]. While the MJO subjects the extratropics to variability they would not otherwise experience, it also helps "anchor" capricious extratropical weather, providing an important source of predictability on weekly to monthly timescales [*Lau and Waliser*, 2012; *Zhang*, 2013]. Even though medium range forecasting still poses significant challenges to the development of seamless prediction suites aimed at bridging the gap between weather and climate, continual advancement in our understanding of the MJO and its teleconnections [*Roundy et al.*, 2010] offers prospects of progress in the years to come [*Zhang*, 2013].

The findings of a growing number of studies, both observational and numerical simulation based, indicate that MJO activity may increase as the climate system warms, suggesting a potential boon for medium range forecasting [*Hand*, 2015]. The findings of *Slingo et al.* [1999], *Jones and Carvalho* [2006], and *Oliver and Thompson* [2012], who used reanalysis products to examine historical changes in MJO activity, suggest that increases in MJO activity on decadal or longer timescales may be related to increases in tropical SST. Numerical simulations, ranging from idealized aquaplanet studies [*Lee*, 1999; *Caballero and Huber*, 2010; *Maloney and Xie*, 2013; *Arnold et al.*, 2013; *Carlson and Caballero*, 2016] to more realistic simulations [*Schubert et al.*, 2013; *Arnold et al.*, 2015], have found robust increases in MJO convective activity with increasing SST, though *Maloney and Xie* [2013] highlight that any future changes in the MJO are likely to be sensitive to the spatial pattern of warming. The findings of *Arnold et al.* [2015] are particularly relevant to this study, as the same simulations analyzed in that study will be investigated here. *Arnold et al.* [2015] analyzed MJO activity in two 10 year simulations of the superparameterized NCAR Community Earth System Model (SP-CESM), one at preindustrial levels of CO_2 (280 ppm, hereafter PI) and one where CO_2 levels have been quadrupled (1120 ppm, hereafter $4\times CO_2$). MJO activity was found to increase considerably in both frequency and strength from the PI to $4\times CO_2$ simulation. A column moist static energy (MSE) budget was used to identify the steepening of the mean MSE profile, a robust thermodynamic consequence of warming, as the most likely cause of enhancement in MJO activity. A steepened mean MSE profile makes the export of column MSE by the anomalous circulation less efficient, thereby reducing the stabilizing effect variations in convection have on column MSE. This mechanisms for MJO intensification with warming is supported by the findings of *Carlson and Caballero* [2016], as well as more idealized studies of convective aggregation [*Arnold and Randall*, 2015]. Yet *Pritchard and Yang* [2016] found no significant changes in the effect of vertical MSE advection on the MJO across the temperature range of 25–35°C in their climate sensitivity study of the MJO, affirming the need for further work on this topic. It is also worth emphasizing that only one convection permitting GCM framework (various superparameterized versions of the Community Atmosphere Model) has been used to demonstrate amplification of the MJO with warming to this point, again highlighting the need for further research on this topic.

An alternative framework for understanding the interactions between moisture, convection, and large-scale circulations in the tropics, which provides a more detailed perspective than that provided by the column MSE budget, has been implemented in recent studies of the MJO [*Chikira*, 2014; *Wolding and Maloney*, 2015; *Janiga and Zhang*, 2016; *Wolding et al.*, 2016]. Briefly, these studies use weak temperature gradient (WTG) balance to diagnose large-scale vertical motion from apparent heating [*Sobel et al.*, 2001; *Raymond*, 2001], allowing large-scale vertical moisture advection to be decomposed into contributions from various apparent heating processes (e.g., radiative heating, microphysical processes, etc.). This vertically resolved WTG framework is consistent with the column MSE budget framework, and is akin to quantitatively partitioning the vertical advection term of the column MSE budget into contributions from radiative heating, microphysical processes, and subgrid scale (SGS) eddy transports. A detailed discussion of the physical underpinnings of this framework is provided in *Wolding et al.* [2016]. In addition to providing a more detailed perspective on interactions between moisture, heating, and large-scale circulations, the vertically resolved WTG analysis provides a clear framework for assessing how these interactions are impacted by changes in the mean state static stability and vertical moisture gradient of the tropics, making it an ideal framework for investigating the MJO in a warming climate.

Here we have chosen perform a vertically resolved WTG analysis of the PI and $4\times CO_2$ simulations investigated by *Arnold et al.* [2015]. As these simulations, and the associated changes in the MJO, are well documented in *Arnold et al.* [2015], this allows more focus to be placed on the analysis of unique findings in this

study. In addition, this allows the findings of the vertically resolved WTG balance analysis to be directly compared to the findings of the column MSE analysis implemented by *Arnold et al*. [2015]. This study will focus on the impacts of increased static stability and a steepened vertical moisture gradient, as these features are robust moist thermodynamic responses to warming. The impacts these changes have on the MJO itself, as well as how they impact the MJO's global influence, will be assessed using WTG theory.

This paper is organized as follows. A description of the model, experimental setup, and analysis techniques is provided in section 2. Basic features of both simulations, and changes in the moist thermodynamic structure of the tropics, are presented in section 3. Section 4 will focus on the impacts of changes in static stability. Moisture variance budgets of the PI and $4\times CO_2$ simulations will be compared in section 5, with a focus on the impacts of changes in the moist thermodynamic structure of the tropics. Discussion and conclusions will be provided in section 6.

2. Model Description, Experimental Design, and Method of Analysis

Superparameterization [*Grabowski*, 2001; *Randall et al*., 2003], whereby cloud system-resolving models (CSRMs) are embedded within each column of a general circulation model (GCM) and used to compute tendencies of moisture and temperature resulting from processes occurring on the SGS of the GCM, has several advantages when compared to conventional parameterizations of convection. Deep convection, fractional cloudiness, and cloud overlap are explicitly simulated, allowing for more realistic interactions between radiation, clouds, and the large-scale environment. Additionally, processes occurring on the SGS are coupled to the large-scale in such a way that their individual contributions to large-scale tendencies of moisture and temperature are cleanly separable.

The 10 year PI and $4\times CO_2$ simulations of SP-CESM used in this study are the same used by *Arnold et al*. [2015]. Briefly, this version of SP-CESM implements a two-dimensional version of the System for Atmospheric Modeling (SAM) 6 [*Khairoutdinov and Randall*, 2003], with a single moment bulk microphysics scheme, 32 columns of 4 km width, and 28 vertical levels as the CSRM embedded within each column of the CESM version 1.0.2 [*Hurrell et al*., 2013]. The NCAR Community Atmosphere Model (CAM), run with $1.9°\times 2.5°$ horizontal resolution, with 30 vertical levels, CAM4 physics, and a 15 min time step, serves as the atmospheric component of the CESM, and is coupled to dynamic ocean (POP2) and sea ice (CICE) models with $1.125°\times 0.63°$ resolution. *Arnold et al*. [2015, section 2] provides details of model spin-up, as well as several mean state biases present in the PI simulation.

All season OLR-based EOF indices of the MJO, calculated for both the PI and $4\times CO_2$ simulations, are used to produce composite life cycles of the MJO. Leading EOFs of latitudinally averaged ($15°N-15°S$) 20–100 day band-pass filtered OLR were computed following the methodology that *Kiladis et al*. [2014] used to produce the FMO index. These "FMO-like" indices will hereafter be referred to as FMO indices. The first two EOFs explain 16.7 and 12.4% of the total variance, respectively, for the PI simulation, and 17.6 and 16.3% of the total variance, respectively, for the $4\times CO_2$ simulation. The leading EOFs are well separated based on the criteria of *North et al*. [1982] for both the PI and $4\times CO_2$ simulations. The structures of these EOFs, shown in Figure 1, are consistent with the structures of the OLR components of the multivariate EOF derived by *Wheeler and Hendon* [2004, Figure 1].

Analysis techniques and plotting convections similar to those used by *Wolding et al*. [2016], who provide a detailed analysis of the MJO in the PI simulation, will be implemented when possible to facilitate direct comparison with the results of that study. Moisture budget composite "snapshots" of the $4\times CO_2$ MJO are produced from 19 wintertime (October–April) MJO events, selected using an index of $20-100$ day band-pass filtered OLR, averaged over the area of $10°N-10°S$, $110°E-130°E$. Following the methodology of *Wolding et al*. [2016], events were defined as index minima separated by at least 20 days, where anomalously low OLR (i.e., enhanced convection) caused the index to exceed a 1.5 standard deviation threshold.

As in *Wolding et al*. [2016], intraseasonal moisture variance budgets are used to compare the role that various moisture budget terms play in the destabilization of the MJO in the PI and $4\times CO_2$ simulations. The fractional growth rate of intraseasonal column moisture variance contributed by moisture budget term P is given by
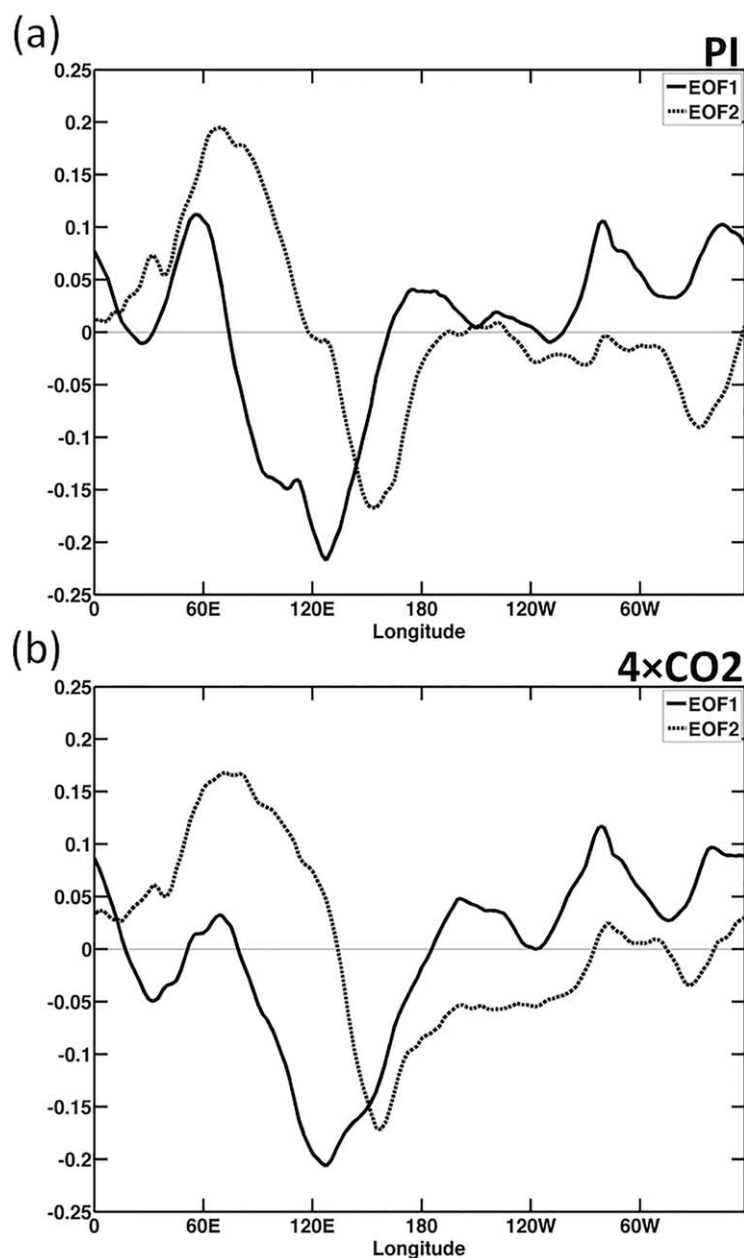
Figure 1. The two leading EOF structures of latitudinally averaged (15°N-15°S) 20–100 day band-pass filtered OLR for the (a) PI and (b) 4×CO$_2$ SP-CESM simulations. The first two EOFs explain 16.7 and 12.4% of the total variance, respectively, for the PI simulation, and 17.6 and 16.3% of the total variance, respectively, for the 4×CO$_2$ simulation.

$$G_P(p,t) = \frac{\int\int P(p)\langle q\rangle dx\, dy}{\int\int \langle q\rangle^2 dx\, dy},$$

(1)

where q is specific humidity that has been band-pass filtered to $20-100$ days, and the angled brackets represent vertical integrals from the surface to 100 hPa. This equation will be vertically integrated over different levels throughout this paper, and the levels of integration will be noted in respective figure captions. As in *Wolding et al.* [2016], the choice was made to project moisture budget term $P(p)$ onto the column-integrated specific humidity $\langle q\rangle$. An alternative approach could be to project moisture budget term $P(p)$ onto the anomalous moisture at each level, $q(p)$, and to subsequently consider the vertical integral of the product of those terms. Although both methods were investigated in this study, the former was chosen on the basis that the SGS effects of convection can vertically redistribute moisture provided by other processes (e.g., radiative heating), such that their influence is distributed throughout the column. Moisture variance budgets for both PI and 4×CO$_2$ simulations are calculated over the domain of 15° N$-$15°S, 60°E$-$180°E for all days when their respective FMO indices exceed a magnitude of 1. Conclusions drawn from this analysis are not sensitive to reasonable changes in the domain or magnitude threshold considered.

MJO phase composites in section 4.1.1 were produced, and their statistical significance assessed, in the following manner. For each phase of the MJO, dates where the magnitude of the FMO index exceeded 1 were selected. These dates were then limited to the months of DJF, when the northern hemisphere extratropical response to MJO heating is particularly strong. Various anomalous fields were composited together for the selected dates for each respective phase, meant to represent anomalous conditions associated with the MJO. Moving-block bootstrap analysis [e.g., *Henderson et al.*, 2016] was used to assess the statistical significance of the composites for each MJO phase, as well as the significance of the average of all eight phase

composites. Specifically, the goal was to assess if the root mean square (RMS) of an anomalous field (e.g., column averaged Q_1) over a given domain (e.g., 15°N−15°S) was significantly larger for a given composite than for randomly sampled days. In other words, the goal was to determine if there was a significant signal associated with the MJO being captured in the composite. A second goal was to test if there was a significant difference between the RMS anomalies of the PI and 4×CO2 simulations. In other words, the goal was to determine if there are significant changes in the strength of some signal associated with the MJO from the PI to 4×CO2 simulation. As in traditional bootstrap analysis, samples were taken with replacement to approximate the distribution and characteristics of the data being used in the composites. As MJO events often spend several consecutive days in a single MJO phase, moving-block bootstrap imposes the additional requirement that samples be chosen in consecutive blocks of length l such that the effect of data auto-correlation is preserved. A bootstrap sample of size N was produced by joining N/l randomly sampled blocks, where N is the number of days used in the composite being assessed, and an l of 5 was used, corresponding to an average persistence of 5 days in each MJO phase, and an average period of 40 days for the entire eight phase MJO lifecycle. This process was repeated 2000 times to obtain bootstrap samples sufficient to represent the distribution and characteristics of the data being used. The size of N for the eight MJO phases composited in the both PI and 4×CO2 simulations is given in the captions of Figures 6 and 7.

3. Changes From PI to 4×CO2

This section will introduce differences between the PI and 4×CO2 simulations that are most relevant to the subsequent sections. As the basic state and intraseasonal variability of both simulations are well documented in *Arnold et al.* [2015, section 3, Figures 1–5], a limited analysis is presented here. Figures 2a and 2c show mean SST and total precipitation variance in the PI simulation. As discussed in *Arnold et al.* [2015], the PI simulation has a ∼1K SST cold bias relative to observations (not shown), a pronounced double ITCZ over the Pacific Ocean, and precipitation variance that is too large over the western Indian Ocean relative to observations (not shown). SST cold biases are a common symptom of models that produce vigorous intraseasonal variability [*Kim et al.*, 2011]. The enhanced precipitation variance in the western Indian Ocean
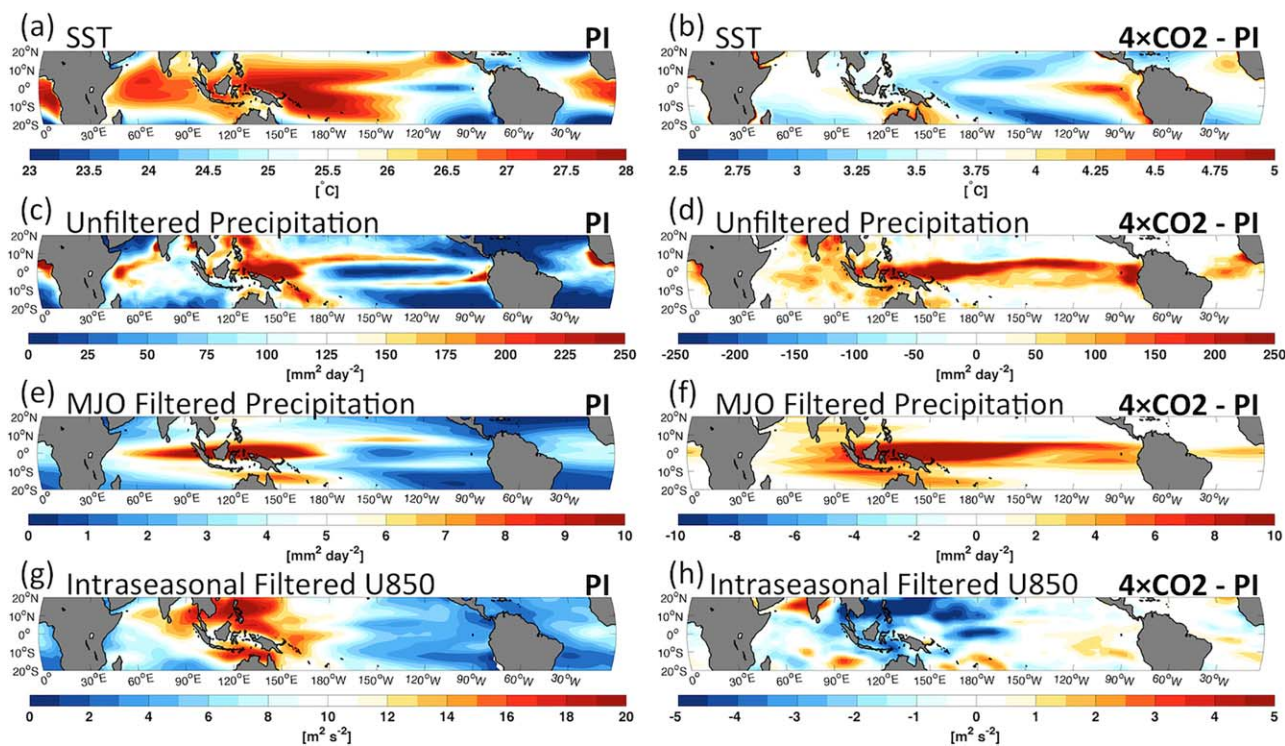

Figure 2. (a, b) Time mean SST, (c, d) variance of unfiltered precipitation variance, (e, f) variance of precipitation filtered to eastward wavenumbers 0–5 and frequencies corresponding to 20–100 days, and (g, h) variance of 20–100 day band-pass filtered 850 hPa zonal wind for the PI simulation, and difference between the 4×CO2 and PI simulations, respectively.
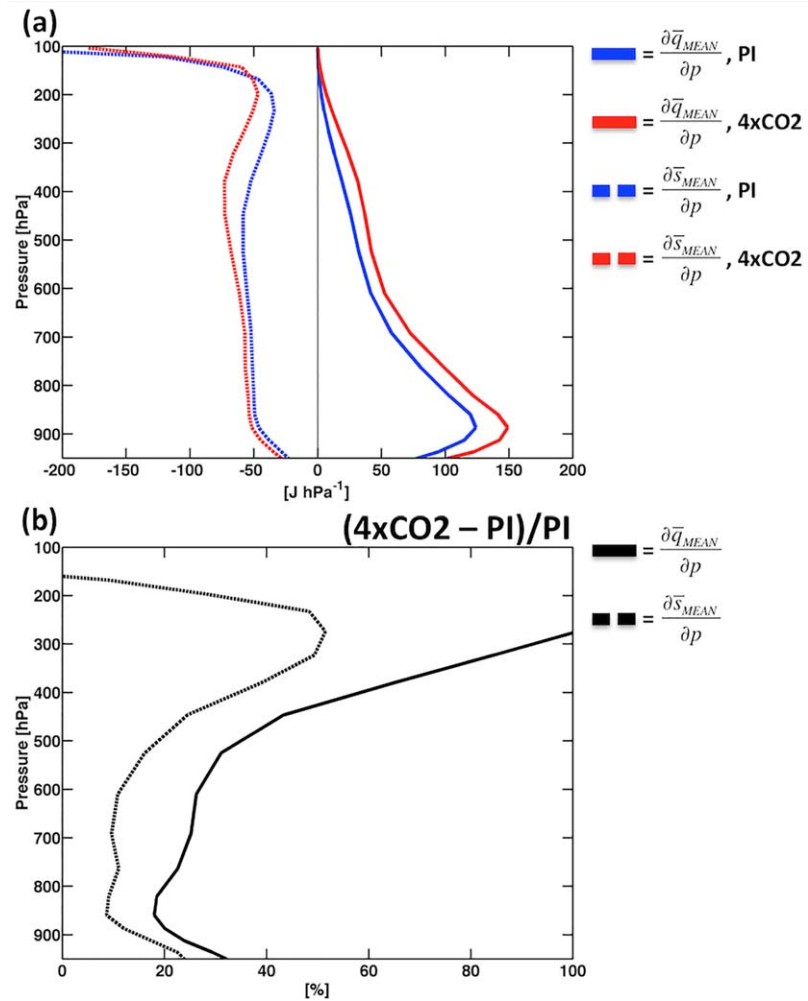
Figure 3. (a) Time mean profiles of the vertical moisture gradient (solid lines) and vertical dry static energy gradient (dashed lines) averaged over the domain $10°N-10°S, 60°E-180°E$ for the PI (blue) and $4\times CO_2$ (red) simulations, and (b) fractional change between the $4\times CO_2$ and PI simulations.

contributes to unrealistic mean state low level easterlies in the Indian Ocean, which affects surface latent heat flux (SLHF) feedbacks to the MJO [*Arnold et al.*, 2015; *Wolding et al.*, 2016]. Figures 2b and 2d show changes in SST and total precipitation variance from the PI to $4\times CO_2$ simulations. SST increases everywhere, but exhibits an El-Nino like pattern of warming. Total precipitation variance increases most dramatically over the Pacific Ocean and has a pattern indicative of an equatorward shift of the northern ITCZ. Figures 2e and 2f show that PI MJO precipitation variance is largest over the Indian and west Pacific Oceans and that MJO precipitation variance more than doubles in most regions in the $4\times CO_2$ simulation. MJO precipitation variance increases most dramatically over the Pacific Ocean, consistent with the increase in total precipitation variance. Figure 2g shows PI intraseasonal zonal wind variance at 850 hPa, which has a longitudinal distribution similar to that of MJO precipitation variance. Interestingly, despite the considerable increase in MJO precipitation variance in the $4\times CO_2$ simulation (Figure 2f), zonal wind variance actually decreases in most areas (Figure 2h). This remarkable change was noted by *Arnold et al.* [2015], and *Maloney and Xie* [2013] used WTG balance to show that similar changes in their aquaplanet simulations were the result of increased tropical static stability with warming. Consequences of this change, and of increasing static stability with warming, will be a primary focus of the next section.

Figure 3a shows vertical profiles of static stability (dashed lines) and the vertical moisture gradient (solid lines) for the PI (blue lines) and $4\times CO_2$ (blue lines) simulations, averaged from $10°N-10°S, 60°E-180°E$. Both static stability and the vertical moisture gradient have increased throughout the depth of the troposphere in the $4\times CO_2$ simulation. Figure 3b shows that static stability (dashed line) increases by around 10%
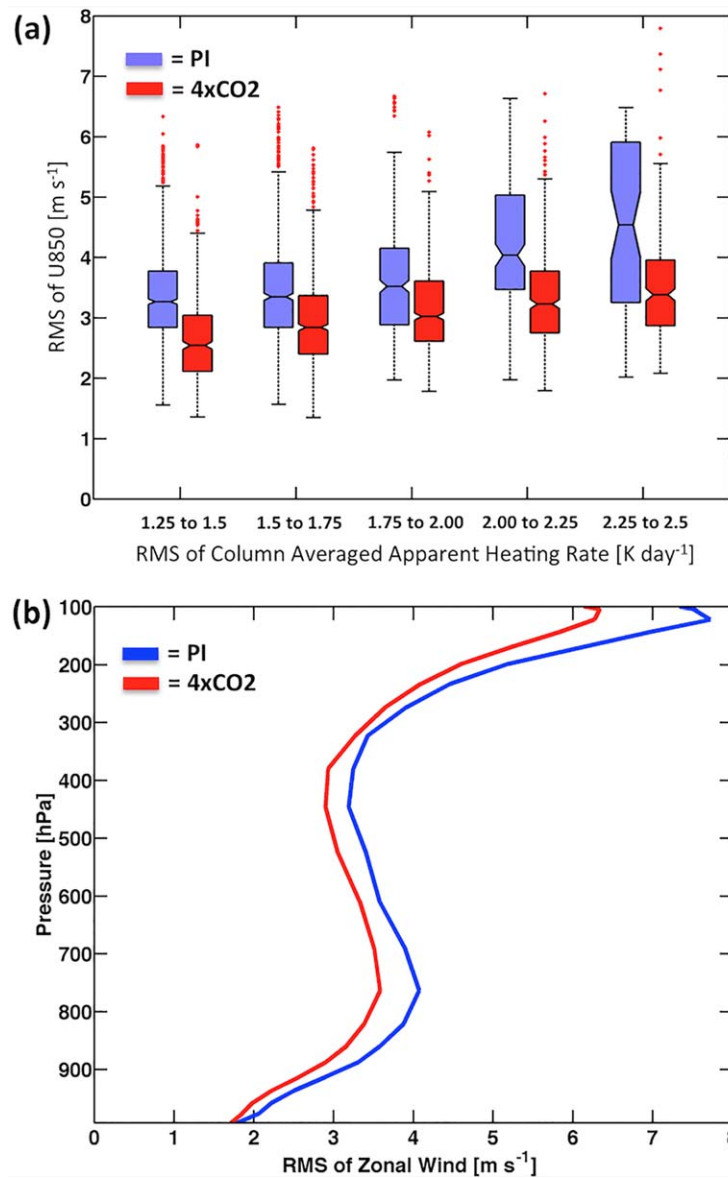
Figure 4. (a) Box and whisker plots of the root mean square (RMS) of 20–100 day band-pass filtered 850 hPa zonal wind for the domain $10°N-10°S$, $60°E-180°E$, binned by the RMS of 20–100 day band-pass filtered column-averaged apparent heating rate over the same domain, for the PI (blue) and $4\times CO_2$ (red) simulations. Medians differ with 95% statistical significance if their notched intervals do not overlap. (b) Vertical profile of the RMS 20–100 day band-pass filtered zonal wind for the 1.75–2.00 K d^{-1} bin in Figure 4a.

in the lower troposphere, and by as much as 50% in the upper troposphere. Similarly, the vertical moisture gradient (solid line) shows the largest percentage increase in the upper troposphere. Subsequent sections will use WTG to investigate how these changes in static stability and the vertical moisture gradient will impact the MJO and its global influence.

4. Implications of Increased Static Stability

The tropics are characterized by weak horizontal gradients of temperature and pressure, a result of effective gravity wave adjustment given the large Rossby radius of deformation. On intraseasonal timescales, the leading order balance in the dry static energy (DSE, s) budget is between apparent heating and adiabatic cooling. This balance is widely referred to as WTG balance, and is given by

$$\bar{\omega}\frac{\partial \bar{s}}{\partial p}=Q_1, \qquad (2)$$

which can be rearranged to give

$$\bar{\omega}=\frac{Q_1}{\frac{\partial \bar{s}}{\partial p}}, \qquad (3)$$
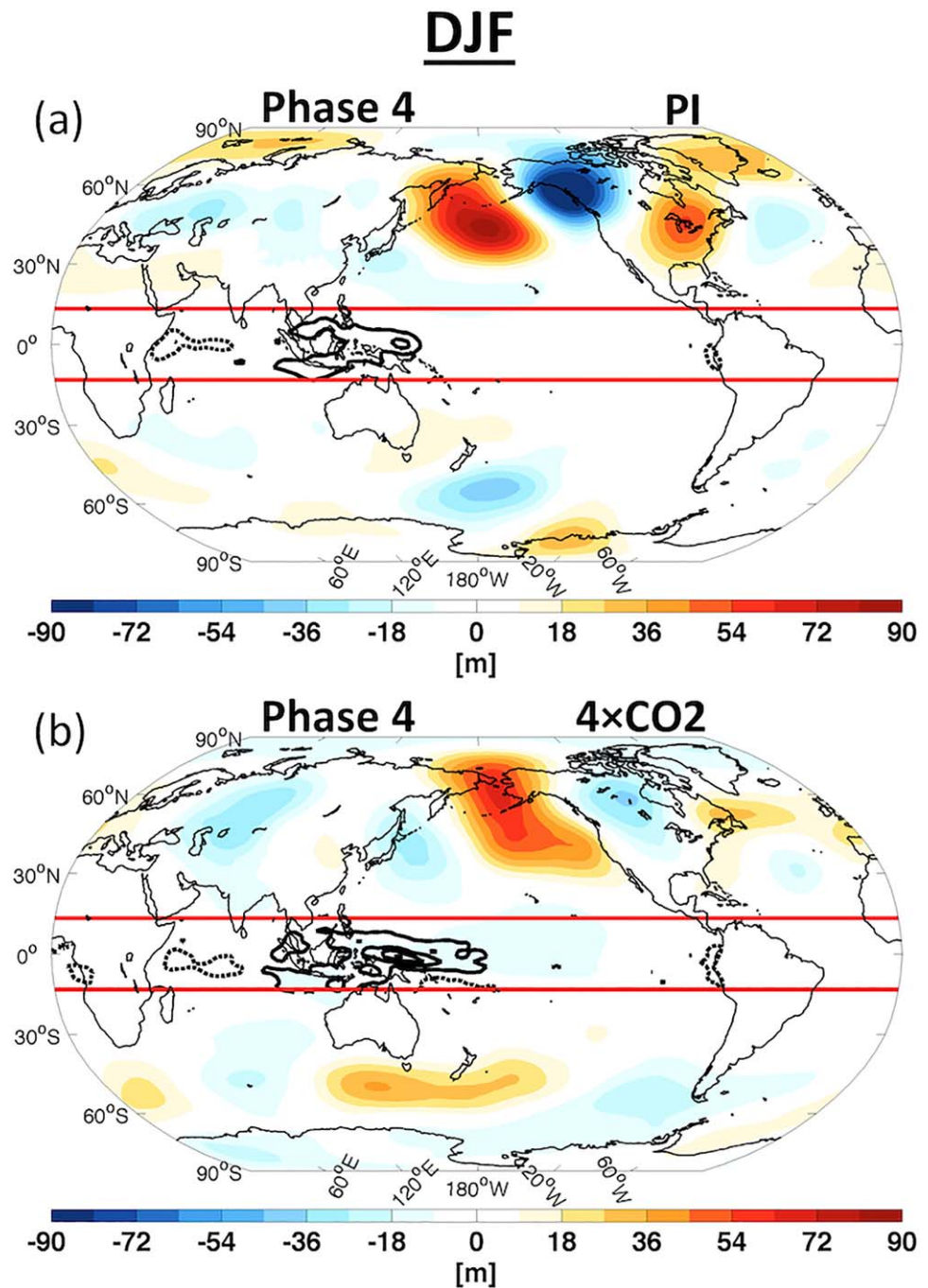
where the overbar indicates the large-scale average of a

quantity and Q_1 is the apparent heat source [*Yanai et al.*, 1973]. In the context of the MJO, this paper takes the perspective that intraseasonal variations in large-scale vertical motion are the result of effective gravity wave adjustment occurring on temporal scales much shorter than, and spatial scales much larger than, intraseasonal variations in apparent heating. Inspection of equation (3) indicates that static stability serves as a measure of dynamic sensitivity to apparent heating, determining the large-scale vertical velocity required for adiabatic cooling to balance apparent heating. This relationship holds to a high degree of accuracy in both the PI [see *Wolding et al.*, 2016, Figure 6] and $4\times CO_2$ (see Figure A1) simulations. As static stability increases, the large-scale velocity required to balance a given amount of apparent heating decreases [*Knutson and Manabe*, 1995; *Held and Soden*, 2006]. Given that large-scale vertical velocity results from horizontal convergence and divergence acting throughout the column, it follows that the horizontal wind response to apparent heating may also decrease as static stability increases [*Maloney and Xie*, 2013].

Figure 5. DJF phase 4 composites of 20–100 day band-pass filtered column-averaged apparent heating anomalies (contours) in the tropics, and 20–100 day band-pass filtered 525 hPa geopotential height anomalies (color shading) in the extratropics for the (a) PI and (b) $4\times CO_2$ simulations. Red lines at 15°N and 15°S denote the boundaries used for tropical and extratropical averaging in the corresponding analysis. Solid and dashed contours correspond to positive and negative heating rates, respectively, contoured every 2 K d^{-1} starting at ± 1 K d^{-1}, with the 0 K d^{-1} contour omitted.

Figure 4a shows a box and whisker plot of the RMS of 850 hPa zonal wind anomalies for the domain 10°N−10°S, 60°E−180°E, binned by the RMS of column averaged Q_1 anomalies for the same domain. The central mark of each box indicates the median, the bottom and top edges of each box indicate the 25th and 75th percentiles, respectively, the whiskers extend to the most extreme data points not considered outliers, and red markers indicate outliers that are more than 1.5 times beyond the interquartile range of the lower and upper quartiles. Medians differ with 95% statistical significance if their notched intervals do not
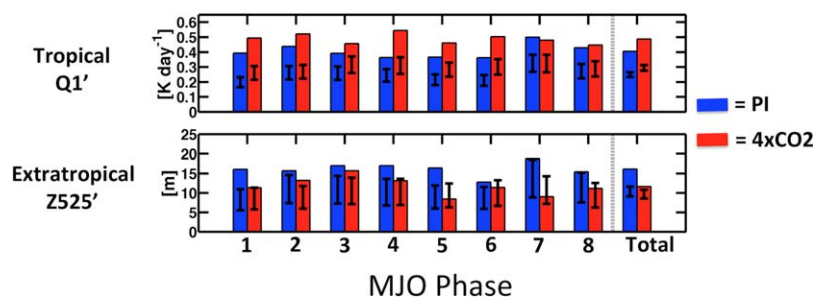
Figure 6. Root mean square (RMS) of tropical 20–100 day band-pass filtered column-averaged apparent heating anomalies (top) and northern hemisphere extratropical 20–100 day band-pass filtered 525 hPa geopotential height anomalies (bottom) for composites of each MJO phase, and the average across all eight phase composites for the PI (blue) and $4 \times CO_2$ (red) simulations. Tropical and extratropical averaging occurs equatorward and poleward of 15°N and 15°S, respectively. Brackets indicate the 95% confidence intervals, determined using the moving block bootstrapping analysis described in section 2. Bootstrap sample size N, corresponding to the number of days in each phase composite, is equal to 101, 57, 59, 66, 86, 89, 36, and 52 for phases 1 through 8 of the PI simulation. Bootstrap sample size N is equal to 84, 78, 56, 58, 71, 62, 54, and 69 for phases 1 through 8 of the $4 \times CO_2$ simulation.

overlap. Figure 4a indicates that the same amount of heating consistently produces a weaker zonal wind response in the $4 \times CO_2$ simulation (red boxes) than the PI simulation (blue boxes), with the median values of the former being less than the latter with 95% statistical significance for each bin considered. Figure 4b, which shows a vertical profile of the domain RMS zonal wind anomalies for the 1.75–2.00 K d^{-1} bin, indicates that the zonal wind response to a given amount of heating is weaker at all levels in the $4 \times CO_2$ simulation (red line) than in the PI simulation (blue line). This suggests that changes in zonal wind variance at 850 hPa (Figure 2h) are not simply a result of changes in the vertical structure of Q_1 and that the dynamical response to intraseasonal variations in heating is consistently weaker throughout the column in the $4 \times CO_2$ simulation. This is consistent with the findings of *Pritchard and Bretherton* [2014], who noted a weakening of the dynamic anomalies associated with the MJO despite the amplification of its convective signature in a simulation where static stability had been inadvertently increased. It is worth noting that the increased MJO activity in the $4 \times CO_2$ simulation is accompanied by an increase in column averaged Q_1 anomalies, partially counteracting the weakened dynamical response to variations in heating. As will be shown in subsequent sections, a reduced dynamical response to variations in apparent heating has implications for the MJO itself, as well as implication for how the MJO forces the extratropics.

4.1. Communication Breakdown: Implications for MJO Forcing of the Extratropics

The ability of variations in tropical heating to force the extratropics through the excitation of stationary Rossby wave trains [*Hoskins and Karoly*, 1981; *Sardeshmukh and Hoskins*, 1988; *Hoskins and Ambrizzi*, 1993; *Jin and Hoskins*, 1995; *Trenberth et al.*, 1998] is closely related to anomalous divergence occurring in the presence of mean state absolute vorticity, as well as the advection of mean state absolute vorticity by the divergent part of the anomalous wind [*Sardeshmukh and Hoskins*, 1988]. As increased tropical static stability results in a decreased horizontal wind response to intraseasonal variations of apparent heating, it follows that the MJO's ability to excite an extratropical response may also decrease in a warming climate. Investigating this issue possess significant challenges, as mean state changes (e.g., changes in jet strength and location) and changes in the structure of anomalous heating will influence the ability of variations in tropical heating to force the extratropics. Two different approaches are employed in this section in an attempt to address this issue.

4.1.1. Composite Analysis of SP-CESM Simulations

To aid understanding of subsequent analysis, begin by considering Figure 5, which shows DJF phase 4 MJO composites of column averaged Q_1 anomalies (contours) for the tropics and 525 hPa geopotential height (Z525) anomalies (shading) for the extratropics in the PI (top) and $4 \times CO_2$ simulations (bottom). The red lines located at 15°N and 15°S are used to indicate regions used for averaging in the subsequent analysis, where tropical averaging occurs equatorward of the lines and extratropical averaging occurs poleward of the lines. The months of DJF were chosen because of the strong northern hemisphere (NH) extratropical response to MJO heating at this time, and the 525 hPa level was chosen to facilitate comparison with previous studies of the MJO teleconnection patterns [*Lin et al.*, 2009; *Henderson et al.*, 2016], which is commonly defined at this level. First note that anomalous heating near the maritime continent is much greater in the

$4\times CO_2$ simulation than the PI simulation. This is consistent with the increased strength of the MJO in the $4\times CO_2$ simulation which *Arnold et al.* [2015] documented. The RMS of phase 4 column averaged Q_1 anomalies in the tropics has increased by 0.18 K d^{-1}, a 50% increase from the PI simulation. Now consider the NH extratropical response to the anomalous tropical heating, which appears to have both shifted and weakened in the $4\times CO_2$ simulation, despite the aforementioned increase in anomalous heating. The RMS of phase 4 NH extratropical Z525 anomalies has decreased by 3.8 m, a 23% decrease from the PI simulation.

Similar calculations were done for each of the eight phase composites of the MJO, as well as the average across the eight phase composites. Figure 6 shows the RMS of column averaged Q_1 anomalies for the tropics (top) and the RMS of NH extratropical Z525 anomalies (bottom) for the PI (blue) and $4\times CO_2$ (red) simulations. Dark brackets indicate the 95% confidence bounds, calculated using the bootstrapping methodology detailed in section 2. Composite values that exceed the upper bracket are significantly larger than values obtained by compositing together randomly sampled days, indicating that there is a significant signal associated with the MJO being captured in the composite. First note that for all eight phases of both simulations, tropical Q_1 anomalies exceed the upper bracket of the 95% bounds. This provides confidence that we are sampling heating associated with the MJO, and not simply background intraseasonal Q_1 anomalies. For seven of the eight phases, tropical Q_1 anomalies are greater in the $4\times CO_2$ simulation than in the PI simulation, consistent with the strengthening of the MJO in the $4\times CO_2$ simulation. The RMS of NH extratropical Z525 anomalies (bottom) exceeds the 95% bounds for each of the eight phases for the PI simulation (blue bars), but does so only in phases 2 and 3 of the $4\times CO_2$ simulation. This indicates the extratropical response to MJO heating anomalies is only strong enough to exceed background Z525 anomalies in phases 2 and 3 in the $4\times CO_2$ simulation. In other words, MJO forcing of the extratropics is clearly discernible in the PI simulation, but is much less discernible in the $4\times CO_2$ simulation. This comes as a result of the reduction in extratropical Z525 anomalies from the PI to the $4\times CO_2$ simulation, which occurs in each of the eight phases. Considering the average across all eight phases, extratropical Z525 anomalies are significant in both the PI and $4\times CO_2$ simulation.

To test the significance of the changes in tropical Q_1 and extratropical Z525 anomalies, a bootstrap analysis was performed on both the absolute changes and fractional changes, shown in Figure 7. Composite values exceeding the upper or lower brackets indicate that changes between the PI and $4\times CO_2$ simulation are significantly larger than changes obtained by compositing randomly sampled days for each simulation. In other words, absolute and/or fractional changes associated with the MJO are greater than those occurring in background intraseasonal anomalies. Of the individual phases, only phases 2 and 4 show statistically significant absolute increases in tropical Q_1 anomalies (Figure 7a), but the average absolute increase across all eight phases is statistically significant, consistent with the documented increases in the MJO strength [*Arnold et al.*, 2015]. The tendency for the brackets to be centered above the zero value indicates that background intraseasonal Q_1 anomalies increase from the PI to $4\times CO_2$ simulation. As a percentage increase (Figure 7b), composite changes are not significant for any individual phase, nor are they significant for the average across all eight phases. In other words, while a statistically significant increase in MJO Q_1 anomalies occurs, the fractional increase (i.e., rate of increase) in MJO Q_1 anomalies is not significantly greater than that of background intraseasonal Q_1 anomalies. *Pritchard and Yang* [2016] similarly found that MJO precipitation variability remained an approximately invariant fraction of tropical mean precipitation variability across a wide range of climates. Of the individual phases, phases 1, 5, and 7 show statistically significant absolute decreases in extratropical Z525 anomalies (Figure 7c). Considering the average change across all eight phases, both the absolute decrease (Figure 7c) and fractional decrease (Figure 7d) in extratropical Z525 anomalies are significant. Similar decreases in extratropical geopotential height anomalies occur at all levels throughout the column (not shown), though it is worth noting that the level of maximum geopotential height anomalies shifts slightly upward by around 50 hPa in the $4\times CO_2$ simulation. When considering changes in anomalous extratropical Z525 per tropical Q_1 anomaly (Figures 7e and 7f) (i.e., extratropical response per unit MJO heating), significant absolute and fractional decreases occur in the average across all eight phases, with the latter showing a 40% decrease. In other words, over a complete MJO lifecycle, the ability for anomalous MJO heating to force an extratropical response decreases by 40% from the PI to $4\times CO_2$ simulation.

4.1.2. Mechanism Denial With a Linear Baroclinic Model

As an alternative approach to the composite analysis above, the dry linear baroclinic model (LBM) of *Watanabe and Kimoto* [2000] was used to help isolate the effects of changes in static stability on MJO forcing of
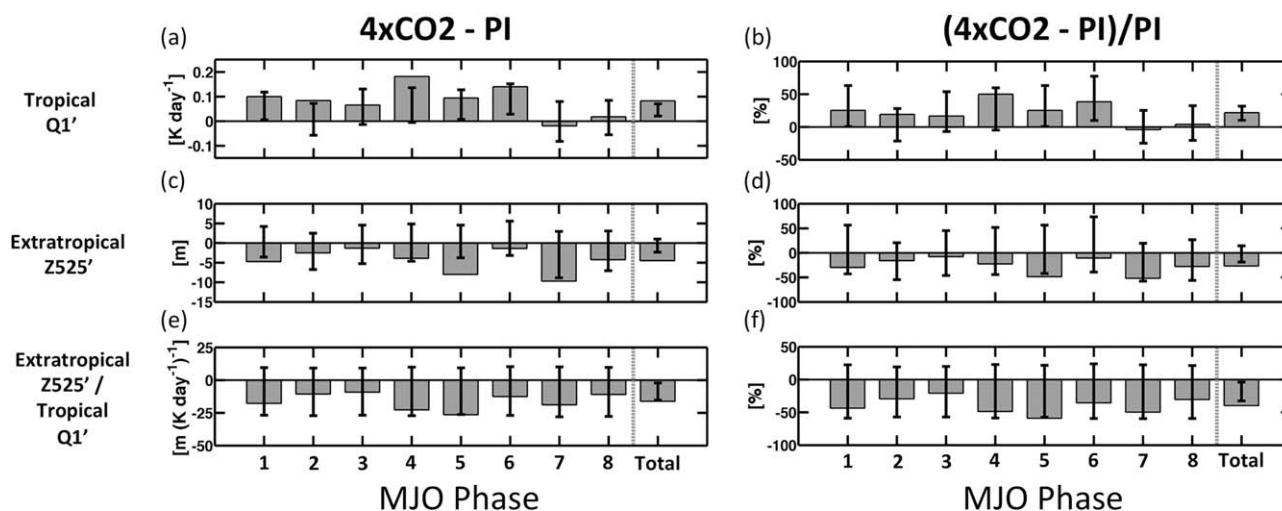
Figure 7. Absolute (left) and fractional (right) changes in the root mean square (RMS) of tropical 20–100 day band-pass filtered column-averaged apparent heating anomalies (top), RMS of northern hemisphere extratropical 20–100 day band-pass filtered 525 hPa geopotential height anomalies (middle), and the ratio of the two (bottom) for composites of each MJO phase, and the average across all eight phase composites. Tropical and extratropical averaging occurs equatorward and poleward of $15°N$ and $15°S$, respectively. Brackets indicate the 95% confidence intervals, determined using the moving block bootstrapping analysis described in section 2. Bootstrap sample size N, corresponding to the number of days in each phase composite, is equal to 101, 57, 59, 66, 86, 89, 36, and 52 for phases 1 through 8 of the PI simulation. Bootstrap sample size N is equal to 84, 78, 56, 58, 71, 62, 54, and 69 for phases 1 through 8 of the $4\times CO_2$ simulation.

the extratropics. This model linearizes the hydrostatic primitive equations on a sphere around a user provided basic state that includes profiles of DSE and horizontal winds, and calculates a steady linear response to a user prescribed steady heating. Four initial simulations were performed, all using the PI phase 3 DJF composite anomalous apparent heating, limited to $15°N-15°S$, as the prescribed heating. The control simulation uses the full PI DJF basic state. The second simulation, which seeks to isolate the effect of changes in horizontal winds, uses the PI DJF basic state with the exception of horizontal winds, which were from the $4\times CO_2$ simulation. The third simulation, which seeks to isolate the effect of changes in DSE (i.e., changes in static stability), uses the PI DJF basic state with the exception of DSE, which is from the $4\times CO_2$ simulation. The fourth simulation uses the full $4\times CO_2$ DJF basic state. Each simulation was run for 34 days, and the 500 hPa geopotential height anomaly response was calculated as the average from days 20–34. Each simulation was performed at T42 horizontal resolution, with 20 vertical sigma levels. An e-folding timescale of 2 h was used for horizontal diffusion at the largest wave numbers, and a Newtonian damping timescale of $(20\,\text{days})^{-1}$ was used for all levels except the lowest and highest, which used a $(0.5\,\text{day})^{-1}$ damping timescale.

The control simulation (Figure 8a), which uses the PI basic state, produces NH extratropical Z525 anomalies that have pattern similar to the phase 4 composites of the PI simulation (Figure 5a), though of lesser magnitude. The LBM response to phase 3 heating most closely matches PI phase 4 composites because the former is an approximate steady state response to stationary heating anomalies, while the latter reflects an evolving response to an eastward moving anomalous heat source (i.e., the eastward propagating MJO). In the second simulation, which seeks to isolate the effects of changes in basic state winds (Figure 8b), the resulting pattern of NH extratropical Z525 anomalies shifts, but the Z525 anomalies show relatively little change in strength. In the third simulation, which seeks to isolate the effects of changes in basic state DSE (i.e., changes in static stability) (Figure 8c), the resulting pattern of NH extratropical Z525 anomalies matches that of the control run, but the Z525 anomalies are considerably weakened. In other words, only the strength of the extratropical response changes. In the fourth simulation, which uses the $4\times CO_2$ basic state are used (i.e., winds and static stability change) (Figure 8d), the pattern of NH extratropical Z525 anomalies both shifts and weakens.

Comparing the two simulations that used the PI basic state winds (i.e., Figures 8a and 8c, left), the RMS of NH extratropical Z525 anomalies decreased by 35% from the PI to $4\times CO_2$ basic state DSE (i.e., Figures 8a–8c, from top left to bottom left). In other words, the strength of the extratropical response decreased by 35% when the static stability increased. Comparing the two simulations that used the $4\times CO_2$ basic state winds (i.e., Figures 8b and 8d, right), the RMS of NH extratropical Z525 anomalies decreased by 36% from the PI to $4\times CO_2$ basic state DSE (i.e., from top right to bottom right, Figures 8b–8d). In other words, the strength of the
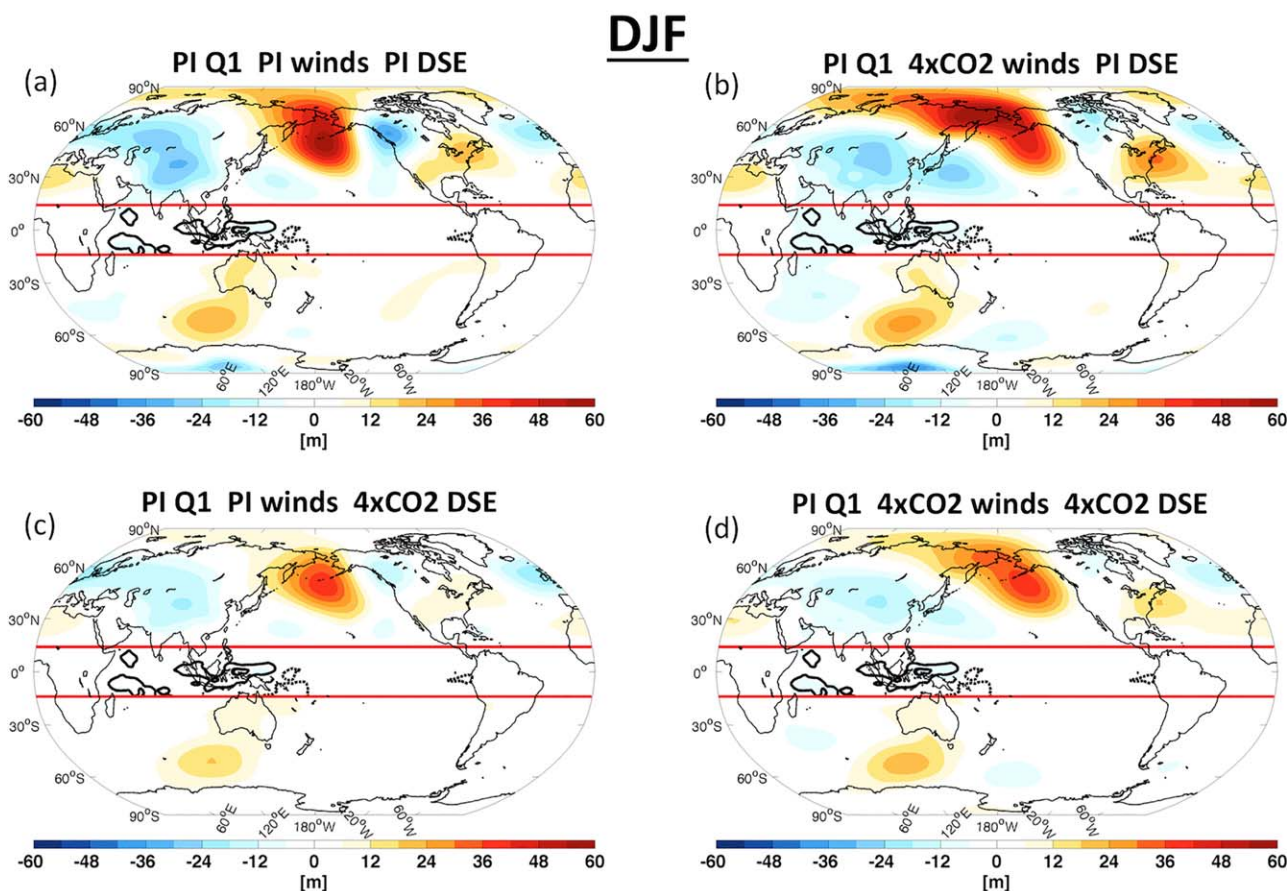
Figure 8. 500 hPa geopotential height anomaly (shading) response of the dry linear baroclinic model (LBM) of *Watanabe and Kimoto* [2000], averaged from days 20 to 34, for four simulations. Each simulation was forced with DJF phase 3 composite column averaged apparent heating anomalies (contours) within the domain of 15°N and 15°S, denoted by the red lines. Basic state fields required by the model include horizontal winds and dry static energy (DSE). (a) Simulation using full PI DJF basic state. (b) Simulation using the PI DJF basic state, with the exception of horizontal winds, which were from the 4×CO₂ simulation. (c) Simulation using the PI DJF basic state, with the exception of DSE, which was from the 4×CO₂ simulation. (d) Simulation using the 4×CO₂ DJF basic state. More details of the LBM and the simulations are provided in section 4.1.2. Solid and dashed contours correspond to positive and negative heating rates, respectively, contoured every 2 K d⁻¹ starting at ±1 K d⁻¹, with the 0 K d⁻¹ contour omitted.

extratropical response decreased by 36% when the static stability increased. These reductions are very close to the 40% reduction in the DJF extratropical response per unit MJO heating observed in SP-CESM.

The same analysis was performed on a second set of four simulations, where each used JJA phase 3 composite Q_1 anomalies and JJA basic state fields (not shown). Comparing the two JJA simulations that used the PI basic state winds, the RMS of SH extratropical Z525 anomalies decreased by 27% from the PI to 4×CO₂ basic state DSE. Comparing the two JJA simulations that used the 4×CO₂ basic state winds, the RMS of SH extratropical Z525 anomalies decreased by 32% from the PI to 4×CO₂ basic state DSE. Equation (3) suggests that a 40% increase in static stability, roughly that which occurs near the levels of peak anomalous heating in SP-CESM (Figure 3b), would reduce the anomalous large-scale vertical velocity produced by a given amount of heating by roughly 30%. The pattern of static stability increase (Figure 3b), which is largest near levels of peak anomalous heating and anomalous vertical velocity, would also contribute to weakening anomalous divergence associated with MJO convective heating. While not conclusive, the results of this section support the idea that increasing static stability reduces the ability of anomalous tropical heating to induce an extratropical Rossby wave response.

5. Implications of Increased Sensitivity of Large-Scale Vertical Moisture Advection to Apparent Heating

Detailed moisture and moisture variance budget analyses were performed as part of this study, and the moisture variance budget has been included in the Appendix for the interested reader. Results of these
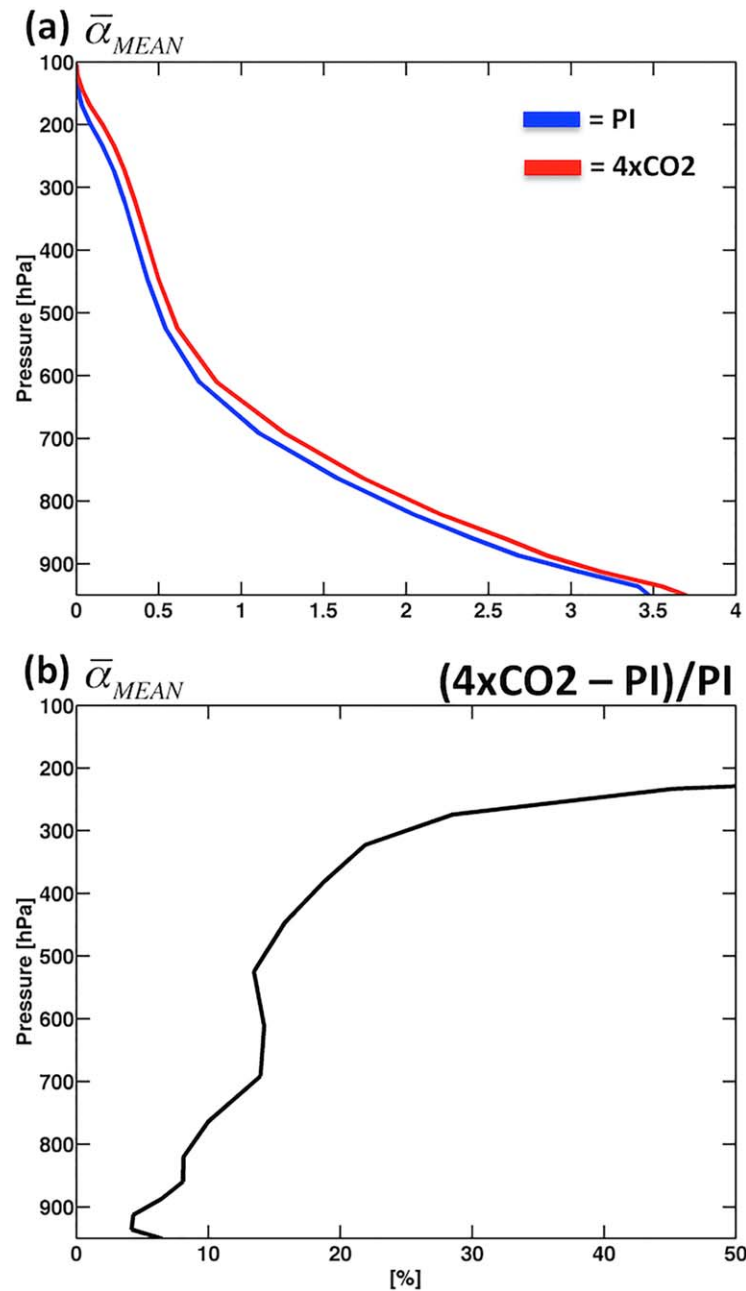
Figure 9. (a) Time mean profiles of $\bar{\alpha}$ (see equation (6)) averaged over the domain $10°N−10°S$, $60°E−180°E$ for the PI (blue) and $4\times CO_2$ (red) simulations, and (b) fractional change between the $4\times CO_2$ and PI simulations.

analyses indicate that the balance of processes acting to destabilize the MJO undergoes relatively small changes from the PI to $4\times CO_2$ simulation, consistent with the findings of *Arnold et al.* [2015]. This section will not address these changes, but will instead focus on how changes in the mean state moist thermodynamic structure of the tropics help support enhanced MJO activity in the $4\times CO_2$ simulation.

Consider the moisture budget, given by

$$\frac{\partial \bar{q}}{\partial t} = -V_h \cdot \nabla \bar{q} - \bar{\omega} \frac{\partial \bar{q}}{\partial p}$$
$$+ \bar{M} - \frac{\partial \overline{\omega' q'}}{\partial p}, \quad (4)$$

where the overbar and prime indicate the large-scale average of a quantity and deviations from the area average respectively, V_h and ω are the horizontal and vertical winds, respectively, q is specific humidity, and M is the moisture tendency due to microphysical processes. Following the vertically resolved WTG framework developed in recent studies [*Chikira*, 2014; *Wolding and Maloney*, 2015; *Janiga and Zhang*, 2016; *Wolding et al.*, 2016], equation (3) can be used to relate large-scale vertical moisture advection to apparent heating, such that

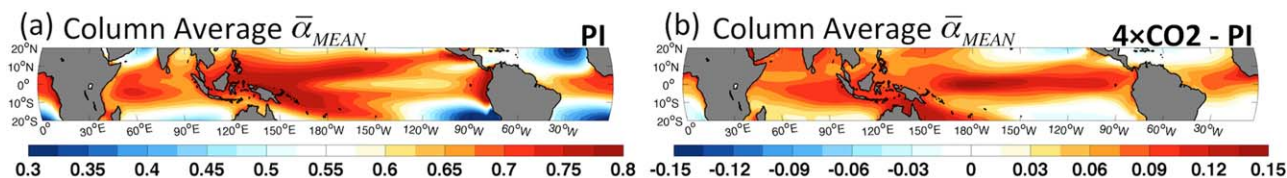$$-\bar{\omega} \frac{\partial \bar{q}}{\partial p} = \bar{\alpha} Q_1, \quad (5)$$

where

$$\bar{\alpha} = -L_v \left(\frac{\frac{\partial \bar{q}}{\partial p}}{\frac{\partial \bar{s}}{\partial p}} \right), \quad (6)$$

and

$$Q_1 = \bar{Q}_M + \bar{Q}_R - \frac{\partial \overline{\omega' s'}}{\partial p}. \quad (7)$$

Figure 10. Time mean $\bar{\alpha}$, averaged from 850 to 100 hPa, for the (a) PI simulation, and (b) difference between the 4×CO$_2$ and PI simulations.

Q_M and Q_R are the DSE tendency due to microphysics and radiation, respectively. Inspection of equation (5) indicates that apparent heating will drive more large-scale vertical moisture advection in a moist thermodynamic environment with a larger $\bar{\alpha}$ [*Chikira*, 2014]. In that sense, $\bar{\alpha}$ serves as a measure of the sensitivity of large-scale vertical moisture advection to apparent heating (see *Wolding et al.* [2016] for more discussion of $\bar{\alpha}$). Given that variations in large-scale vertical moisture advection plays a crucial role in destabilizing the MJO, changes in $\bar{\alpha}$ caused by a warming climate are of considerable interest.

Increases in static stability and the vertical moisture gradient in the 4×CO$_2$ simulation (Figure 3) have opposing effects on $\bar{\alpha}$ (equation (6)). Increased static stability reduces the large-scale vertical velocity produced per unit apparent heating (equation (3)), but the steepened vertical moisture gradient increases the moisture advected by that vertical velocity. The effect of the increased vertical moisture gradient wins out in the 4×CO$_2$ simulation, resulting in an increase in $\bar{\alpha}$ throughout the troposphere (Figure 9). In other words, at a given level, variations in apparent heating will drive stronger variations in large-scale vertical moisture advection in the 4×CO$_2$ simulation. Absolute changes in $\bar{\alpha}$ are largest in the middle troposphere (Figure 9a), while fractional changes in $\bar{\alpha}$ are smallest in the lower troposphere and increase with height (Figure 9b). Column averaged $\bar{\alpha}$ increases across most of the tropics in the 4×CO$_2$ simulation (Figure 10), with the largest increases occurring in regions where precipitation variance has increased the most (Figure 2d).

To illustrate why this increase in $\bar{\alpha}$ may play a crucial role in supporting the increased strength of the MJO, consider the composite moisture budget of the MJO in the 4×CO$_2$ simulation, shown in Figure 11. To facilitate comparison of PI and 4×CO$_2$ moisture budgets, Figure 11 was produced following the same methodology and plotting conventions that *Wolding et al.* [2016] used to analyze the PI moisture budget (their Figure 3). Specific humidity anomalies (contours) indicate that much of the free troposphere is anomalously moist from ~110°E−160°E, consistent with the enhanced phase of the MJO. As in the PI simulation [*Wolding et al.*, 2016], anomalous moistening (color shading) by large-scale vertical moisture advection (Figure 11c) opposes anomalous drying by microphysical processes and SGS eddy fluxes (Figure 11d). The net effect of these large and opposing processes (Figure 11e), hereafter referred to as the column process [*Chikira*, 2014], results in further moistening of regions that are already moist. This moistening by the column process is crucial to the destabilization of the MJO, and is opposed by horizontal advective drying during the enhanced phase (Figure 11b). Comparing moisture budgets of the PI [*Wolding et al.*, 2016, Figure 3] and 4×CO$_2$ simulations shows that moistening by the column process has increased considerably in the latter (Figure 11e), helping support larger specific humidity anomalies in that simulation. Equation (5) indicates that the increased mean state $\bar{\alpha}$ in the 4×CO$_2$ simulation allows MJO convective heating to drive more large-scale vertical moisture advection, helping support this increased moistening by the column process.

Figure 12a shows the contribution that the increase in mean state $\bar{\alpha}$ makes to the amount of large-scale vertical moisture advection MJO convective heating is able to drive in the 4×CO$_2$ simulation. As a result of the increased mean state $\bar{\alpha}$, MJO convective heating in the 4×CO$_2$ simulation produces considerable additional moistening via large-scale vertical moisture advection, particularly from 700 to 300 hPa. The importance of this additional moistening is evident when it is removed from the column process, as shown in Figure 12b. Figure 12b is equivalent to subtracting Figure 12a from Figure 11e. Without the increased mean state $\bar{\alpha}$, moistening by the column process would become anemic, and would be unable to maintain specific humidity against the increased horizontal advective drying (Figure 11b) in the 4×CO$_2$ simulation.

In order to assess if this result can be generalized over the entire MJO lifecycle for a much broader geographic area, moisture variance budgets were calculated for the PI and 4×CO$_2$ simulations. Figure 13 shows the column process (term D) is acting to increase moisture variance in both the PI and 4×CO$_2$ simulations,
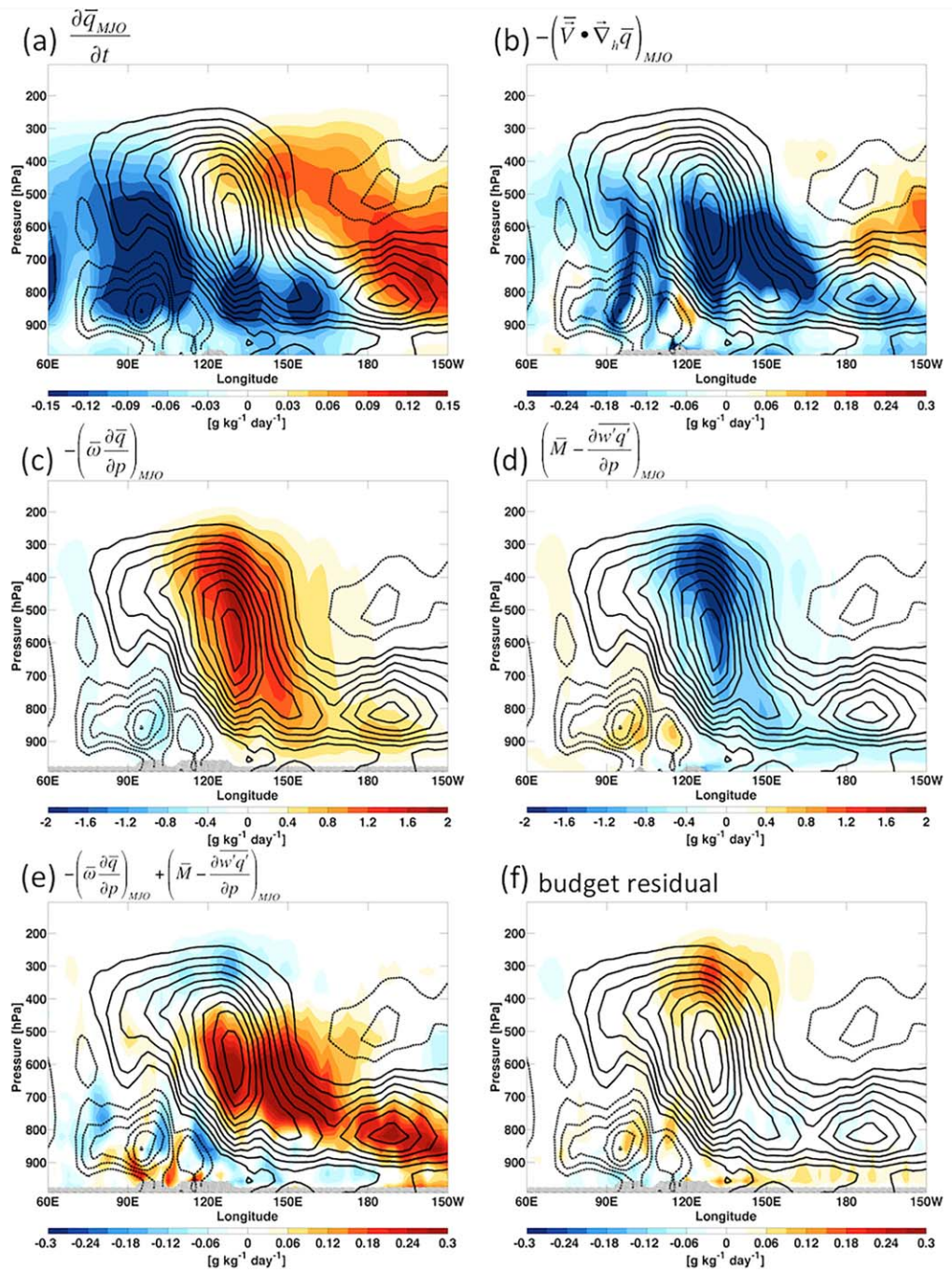
Figure 11. Longitude-height sections of latitudinally averaged (5°N−5°S) composite intraseasonal moisture budget terms (shading) for the 4×CO$_2$ simulation. These terms are the (a) Eulerian moisture tendency, (b) horizontal moisture advection, (c) vertical moisture advection, (d) the net effect of the microphysical moisture tendency and subgrid-scale vertical eddy moisture flux convergence, (e) the column process (i.e., the sum of plots (c) and (d)), and (f) the moisture budget residual. Solid and dashed contours indicate positive and negative specific humidity anomalies, respectively, with contour intervals of 0.1 g kg^{-1}. Composites are produced from 19 independent wintertime (October 1 to April 30) events. Grey hatching indicates regions where data has been lost as a result of proximity to the surface. The subscript MJO indicates application of 20–100 day band-pass filtering. Please note the color scale differs between plots. See *Wolding et al.* [2016, Figure 3] for results of the PI moisture budget, produced following the same methodology and plotting conventions used here.

and that horizontal advection (term C) is acting to damp moisture variance. Remember that each term in the moisture variance budget is normalized by domain averaged moisture variance (see equation (1)), which increases considerably in the 4×CO$_2$ simulation (not shown). Therefore, even though individual moisture budgets terms are much larger in the 4×CO$_2$ simulation (Figure 11), they result in moisture variance
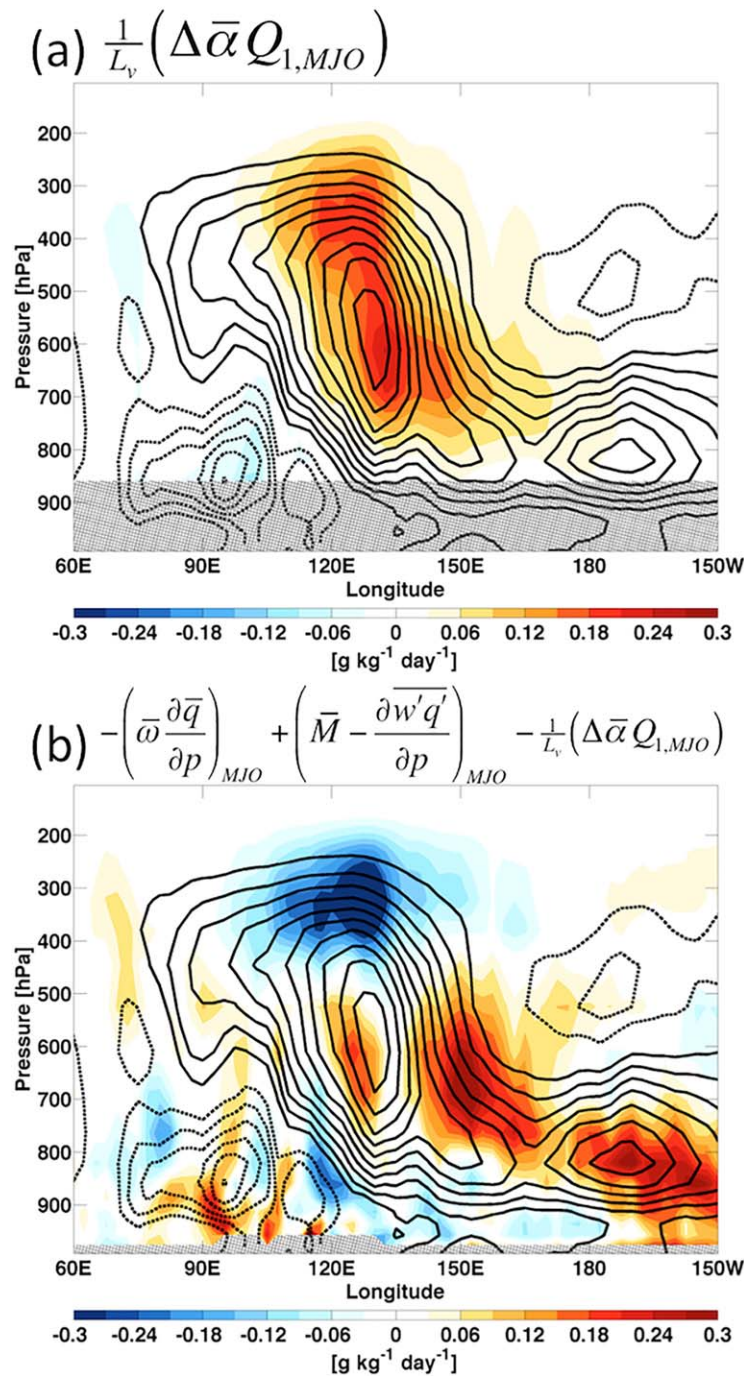
Figure 12. As in Figure 11, except the color shading shows (a) the contribution that changes in time mean $\bar{\alpha}$ between the PI and 4×CO_2 simulation make to large-scale vertical moisture advection in the 4×CO_2 simulation, and (b) the column process without the contribution changes in $\bar{\alpha}$ make to large-scale vertical moisture advection. Figure 12b is equivalent to sub-tracting Figure 12a from Figure 11e. The subscript MJO indicates application of 20–100 day band-pass filtering.

growth rates similar to those of the PI simulation. Interestingly, despite the increased mean state $\bar{\alpha}$ in the 4×CO_2 simulation, destabilization by the column process is weaker in the 4×CO_2 simulation than in the PI simulation (Figure 13, term D). This will be examined further below. For now, consider Figure 14, which shows how MJO moisture variance is affected by the contribution that increased mean state $\bar{\alpha}$ makes to the large-scale vertical moisture advection resulting from total apparent heating (term A), radiative heating (term B), and heating by microphysical processes and SGS eddy fluxes (term C) in the 4×CO_2 simulation. Without the additional large-scale vertical moisture advection resulting from the increased $\bar{\alpha}$ (Figure 14, term A), the column process in the 4×CO_2 simulation (Figure 13, term D) would only be weakly destabilizing, and would not be able to maintain the elevated levels of moisture variance (not shown) against horizontal advective damping (Figure 13, term C). In other words, without the increased mean state $\bar{\alpha}$, MJO convective heating in the 4×CO_2 simulation would not drive sufficient large-scale vertical moisture advection to maintain itself at such elevated levels.

Enhanced MJO convective heating in the 4×CO_2 simulation is accompanied by an increasingly top-heavy heating profile. Figure 15a shows profiles of the RMS of apparent heating anomalies over the entire PI and 4×CO_2 simulations, for the domain 15°N−15°S, 60°E−180°E. Almost all of the additional heating variability in the 4×CO_2 simulation occurs above 500 hPa, and the level of peak heating shifts notably upward. This upward shift may result from a strengthening of the convective anomalies, as well as from more basic energetic and thermodynamic properties of the warmer climate [*Bony et al.*, 2016]. Profiles of RMS radiative heating anomalies (Figure

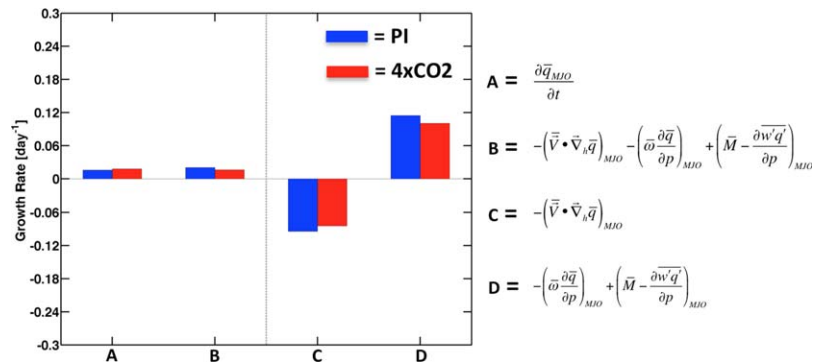**Figure 13.** Vertically integrated contributions various budget terms make to the column moisture variance growth rate in the PI (blue) and $4\times CO_2$ (red) simulations, corresponding to the vertical integral of equation (1). Column moisture was calculated by vertically integrating from the surface to 100 hPa, as were terms A through D. The area weighted integral has been taken from $15°N$-$15°S$, $60°E$-$180°E$, averaged for every day where the magnitude FMO index exceeded a value of 1 for the respective simulations. The subscript MJO indicates application of 20–100 day band-pass filtering.

15b) become more top heavy, yet the upward shift in total apparent heating (Figure 15a) results from change in convective heating to first order. Remember that $\bar{\alpha}$ decreases with height (Figure 9), so this upward shift in peak heating counteracts some of the effect of increased $\bar{\alpha}$. This may help explain why the column process drives slightly weaker moisture variance growth in the $4\times CO_2$ simulation. In short, MJO convective heating occurring in a moist thermodynamic environment with increased $\bar{\alpha}$ is able to more efficiently resupply itself with moisture, supporting enhanced levels of convection. The enhancement of convection is accompanied by a transition to a more top-heavy heating profile, driving down the efficiency with which MJO convection resupplies itself with moisture until its growth is once again limited by horizontal advective damping.

5.1. Comparison With Previous Studies

As previously stated, the vertically resolved WTG framework is consistent with the column-integrated MSE framework used by previous studies of the MJO and climate change [*Arnold et al.*, 2013, 2015; *Carlson and Caballero*, 2016; *Pritchard and Yang*, 2016]. The results of this section support one of the primary conclusions reached by several of these studies, namely that the increase in the mean state vertical MSE gradient in the lower troposphere, and the elevation of the midtropospheric minimum in MSE, help support MJO activity by increasing up-gradient MSE transport via vertical MSE advection [*Arnold et al.*, 2013, 2015; *Carlson and Caballero*, 2016]. The consistency of these results can be highlighted by using the vertically resolved WTG balance framework (see equation (3)) to express large-scale vertical advection of MSE in terms of $\bar{\alpha}$ and Q_1, giving $-\langle \bar{\omega} \frac{\partial \bar{h}}{\partial p} \rangle = \langle Q_1(\bar{\alpha}-1) \rangle$. This study has provided some additional insight to this mechanism, highlighting that increasing $\bar{\alpha}$ in the middle and upper troposphere (Figure 9), where heating variations are large,
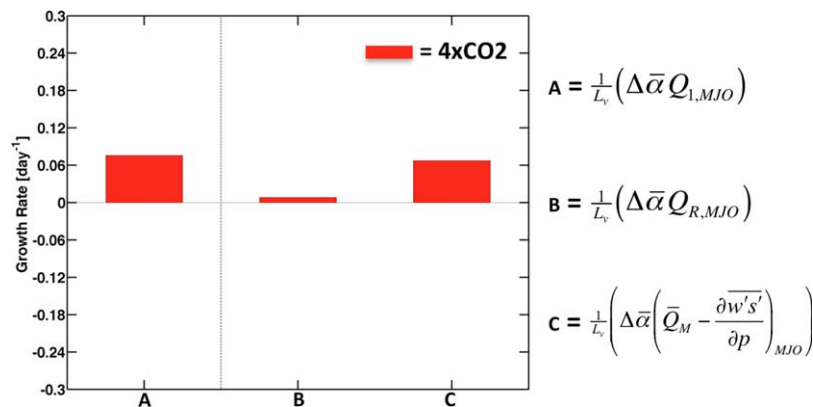

Figure 14. As in Figure 13, except for the contribution that changes in time mean $\bar{\alpha}$ between the PI and $4\times CO_2$ simulation make to large-scale vertical moisture advection resulting from variations in (a) apparent heating, (b) radiative heating, and (c) heating by microphysical processes and SGS eddy fluxes of DSE in the $4\times CO_2$ simulation. All terms were vertically integrated from 850 to 100 hPa, as they depend on the weak temperature gradient approximation.
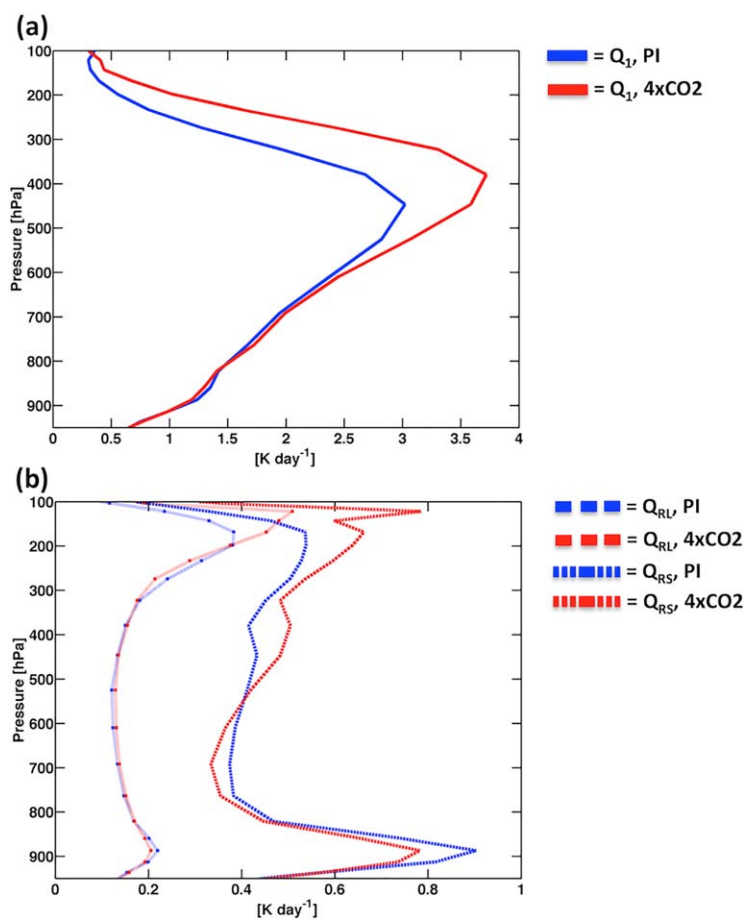
Figure 15. (a) Profiles of the RMS of 20–100 day band-pass filtered apparent heating anomalies, calculated over the entire PI (blue) and $4\times CO_2$ (red) simulations for the domain $15°N−15°S$, $60°E−180°E$. (b) As in Figure 15a, except for longwave (dashed) and shortwave (dot-dashed) radiative heating anomalies.

plays an important role in driving additional large-scale vertical moisture advection in a warming climate. Yet the results of *Pritchard and Yang* [2016], who assessed the climate sensitivity of the MJO across temperatures spanning 1–35°C and found MJO-like variability in even the coldest climates, challenges the notion of a critical temperature threshold for destabilization of the MJO.

Carlson and Caballero [2016] proposed a second mechanisms for MJO intensification, whereby a transition to superrotation in a warming climate allows extratropical eddies to more easily penetrate the tropics, weakening the mean state meridional moisture gradient and reducing the impact of horizontal advective damping of MJO moisture variance by higher-frequency convective variability. This mechanism does not appear to play a role in the $4\times CO_2$ simulation, as no transition toward superrotation is evident in the near

equatorial profile of zonal wind (not shown). Additionally, moisture and moisture variance budgets, provided in the appendix, show no indication of changes in horizontal advective damping by higher-frequency convective variability in the $4\times CO_2$ simulation.

It is also worth highlighting that destabilization by radiative feedbacks, presented in more detail in the Appendix and in Figure A3, weaken slightly in the $4\times CO_2$ simulation. This is consistent with the findings of *Pritchard and Yang* [2016], who found the strength of the radiative feedback decreased considerably with warming in their simulations spanning 1–35°C. While the more top-heavy profile of radiative heating anomalies (Figure 15b) in the $4\times CO_2$ simulation suggests the weakening radiative feedback may be related to changes in the vertical structure of the radiative heating anomalies, the results of *Adames and Kim* [2016] and *Bony et al.* [2016] may provide some additional insight. *Bony et al.* [2016] showed that increased static stability results in the decreased spreading of convective anvils at upper levels in a warming climate, and *Adames and Kim* [2016] demonstrated a scale dependence of the radiative feedback. Further work should be done to identify the mechanism(s) responsible for weakening radiative feedbacks with warming.

6. Discussion

Interactions between convection, large-scale circulations, and moisture are strongly influenced by the moist thermodynamic structure of the environment in which they occur, and such interactions are thought to play an important role in destabilizing the MJO. In this study, the vertically resolved WTG framework has been used to examine how the MJO may be affected by the changing moist thermodynamic structure of

the tropics as the climate system warms. Analysis of two SP-CESM simulations, one at preindustrial levels of CO_2 (280 ppm, hereafter PI) and one where CO_2 levels have been quadrupled (1120 ppm, hereafter $4\times CO_2$), support the following main conclusions:

1. Intraseasonal variations in tropical convective heating will become more efficient at driving variations in large-scale vertical moisture advection as the climate system warms, aiding destabilization of the MJO.
2. Increasing static stability will reduce the dynamical response to intraseasonal variations in tropical convective heating as the climate system warms.
3. The weakening dynamical response to intraseasonal variations in tropical convective heating will reduce the MJO's ability to influence the extratropics as the climate system warms.

Each of these conclusions will now be discussed in turn.

WTG balance provides a useful framework for understanding how changes in static stability and the vertical moisture gradient will alter interactions between convection, large-scale circulations, and moisture as the climate system warms. Increasing static stability and a steepening vertical moisture gradient have opposing effects on the ability of convection to drive large-scale vertical moisture advection. In the $4\times CO_2$ simulation, the effect of the steepened vertical moisture gradient surpasses the effect of increased static stability, allowing variations in convection to drive greater variations in large-scale vertical moisture advection in the warmer climate. This is true throughout the troposphere, with the largest fractional changes occurring in the middle and upper troposphere. The increased variations in large-scale vertical moisture advection promote moisture variance, aiding in the destabilization of the MJO. In other words, the moist thermodynamic environment in the $4\times CO_2$ simulation allows MJO convective heating to more efficiently resupply itself with moisture, supporting elevated levels of convection. This conclusion is consistent with the findings of several previous studies that used the column MSE budget approach [*Arnold et al.*, 2013, 2015; *Carlson and Caballero*, 2016]. The balance of processes acting to destabilize the MJO underwent relatively small changes from the PI to $4\times CO_2$ simulation (see Appendix), lending credence to the notion that increased MJO activity may be a robust response to a warming climate.

Increasing static stability reduces the large-scale vertical velocity required for adiabatic cooling to balance diabatic heating, resulting in a weaker dynamical response to intraseasonal variations in convection in the $4\times CO_2$ simulation. This occurs throughout the troposphere, but is largest in the middle and upper troposphere. As large-scale vertical motion is associated with horizontal convergence/divergence acting throughout the column, a decrease in horizontal wind variance occurs at all levels in the $4\times CO_2$ simulation, consistent with the findings of *Maloney and Xie* [2013].

The reduced dynamical response to MJO convective variability has implications for SLHF feedbacks to the MJO. Surface flux feedbacks to the MJO depend on background low-level winds, to which intraseasonal wind anomalies add constructively or destructively [*Shinoda et al.*, 1998; *Riley Dellaripa and Maloney*, 2015]. Additionally, SLHF feedbacks depend on the absolute air-sea moisture deficit, and the covariance between SLHF anomalies and column moisture anomalies. These dependences present significant challenges to assessing how SLHF feedbacks may change in a warming climate, as realistic assessment of such changes depends not only on accurately simulating these relationships in the current climate, but also on accurately simulating how these relationships will change as the climate system warms. *Arnold et al.* [2015] found that a reduced air-sea moisture deficit contributed to weakened SLHF feedbacks in the $4\times CO_2$ simulation. The results of this study suggest that a weakened dynamical response to MJO convective variability may also contribute to weakened SLHF feedbacks as the climate system warms.

The reduced dynamical response to MJO convective variability also impacts the MJO's ability to influence the extratropics. The excitation of Rossby wave trains by tropical convective variability is closely related to anomalous divergence driven by such variability [*Sardeshmukh and Hoskins*, 1988]. Northern hemisphere (NH) extratropical 525 hPa geopotential height (Z525) anomalies associated with the MJO were shown to be significantly weaker in the $4\times CO_2$ simulation, despite a significant increase in MJO heating anomalies. The ratio of the root mean square (RMS) of NH extratropical Z525 anomalies to RMS anomalous MJO heating was reduced by 40% in the $4\times CO_2$ simulation. In other words, the ability of MJO convective heating to force the extratropics was reduced by roughly 40% in the $4\times CO_2$ simulation. The linear baroclinic model (LBM) of *Watanabe and Kimoto* [2000] was used to isolate the effect of changing static stability on MJO forcing of the extratropics from the effects of changes in climatological winds and changes in the structure of

MJO heating anomalies. Results of the LBM analysis show decreases in the ability of MJO convective heating to force the extratropics that are comparable to those seen in SP-CESM. While not conclusive, the LBM results support the idea that decreases in the ability of MJO convective heating to force the extratropics result from increased tropical static stability.

The MJO drives changes in both means and extremes across the globe, and serves as the primary source of predictability on weekly to monthly timescales. Given the MJO's prominent role in "bridging weather and climate" [*Zhang*, 2005], it is tempting to suppose that, as the climate system warms, increased MJO activity may help ameliorating the medium-range forecasting woes faced by seamless weather prediction efforts. Results of this study suggest that, even though MJO convective heating is likely to increase in a warming climate, the MJO's influence on the extratropics may not. The authors of this study would like to emphasize that the WTG balance relationships discussed here are applicable to phenomena besides the MJO (e.g., ENSO). The WTG balance framework may provide insight to how other phenomena, and their impacts (e.g., ENSO teleconnections), may change as the climate system warms.

Appendix A

A1. Moisture Variance Budget Analysis

Before examining the moisture variance budget, consider Figure A1, which highlights the exceptional accuracy of the vertically resolved WTG framework. Both the anomalous large-scale vertical velocity and anomalous large-scale vertical moisture advection (Figures A1a and A1b) are well diagnosed using WTG balance (Figures A1c and A1d), with very little error (Figures A1e–A1g) being evident throughout the free troposphere. WTG diagnosis of large-scale vertical moisture advection does not work as well in the boundary layer. Therefore, a conservative limit of 850 hPa has been adopted for the vertical integration of terms in the moisture variance budget which depend upon WTG balance.

Figure A2 shows more comprehensive decomposition of the moisture variance budget presented in Figure 13. Remember that moisture variance budget terms are normalized by domain averaged moisture variance (see equation (1)). Therefore, even though individual moisture budgets terms are much larger in the $4\times CO_2$ simulation (Figure 11), they may result in similar growth rates as those in the PI simulation. Comparing the PI and $4\times CO_2$ moisture variance budgets highlights any changes (or lack thereof) in the balance of processes acting to destabilize the MJO. As discussed in section 5, the column process (term D) promotes the growth of moisture variance while horizontal advective damping (term C) limits moisture variance growth, and both terms weaken slightly in the $4\times CO_2$ simulation (red). The column process (term D) can be decomposed in contributions from total radiative heating (term E) and the net effect of microphysical processes and SGS eddy fluxes (term F). The latter (term F) can be further decomposed into contributions from SLHF feedbacks (term G) and SGS convective processes (term H, i.e., convection in the absence of radiative and surface flux feedbacks). Destabilization by both radiative feedbacks (term E) and SGS convective processes (term G) weakens in the $4\times CO_2$ simulation, consistent with the progression to more top-heavy heating profiles discussed in Figure 15, and helping explain the modest weakening of destabilization by the column process (term D). Figure A3 shows the decomposition of the total radiative feedback (term A) into contributions from longwave (term B) and shortwave (term C) components. The modest weakening in destabilization by total radiative feedbacks in the $4\times CO_2$ simulation primarily results from the longwave component (term B), again consistent with the more top-heavy heating profiles discussed in Figure 15. Again, it is worth emphasizing that the weakening radiative feedback may also be related to the mechanisms described by *Bony et al.* [2016], whereby increased static stability results in a decreased spreading of convective anvils at upper levels, or to the scale dependence of the radiative feedback described by *Adames and Kim* [2016]. Taken as a whole, Figure A2 suggests that no large change in the balance of processes acting to destabilize the MJO occurs.

In order to ensure that no large compensating changes occur in the balance of processes acting to destabilize the MJO, horizontal advection and large-scale vertical moisture advection are further decomposed. As in *Chikira* [2014] and *Wolding et al.* [2016], horizontal advection can be decomposed as

$$-\left(V_{\boldsymbol{h}} \cdot \nabla \bar{q}\right)_{MJO} = -\left(V_{\boldsymbol{h},LP20} \cdot \nabla \bar{q}_{LP20}\right)_{MJO} - \left(V_{\boldsymbol{h}} \cdot \nabla \bar{q}\right)_{HF},$$
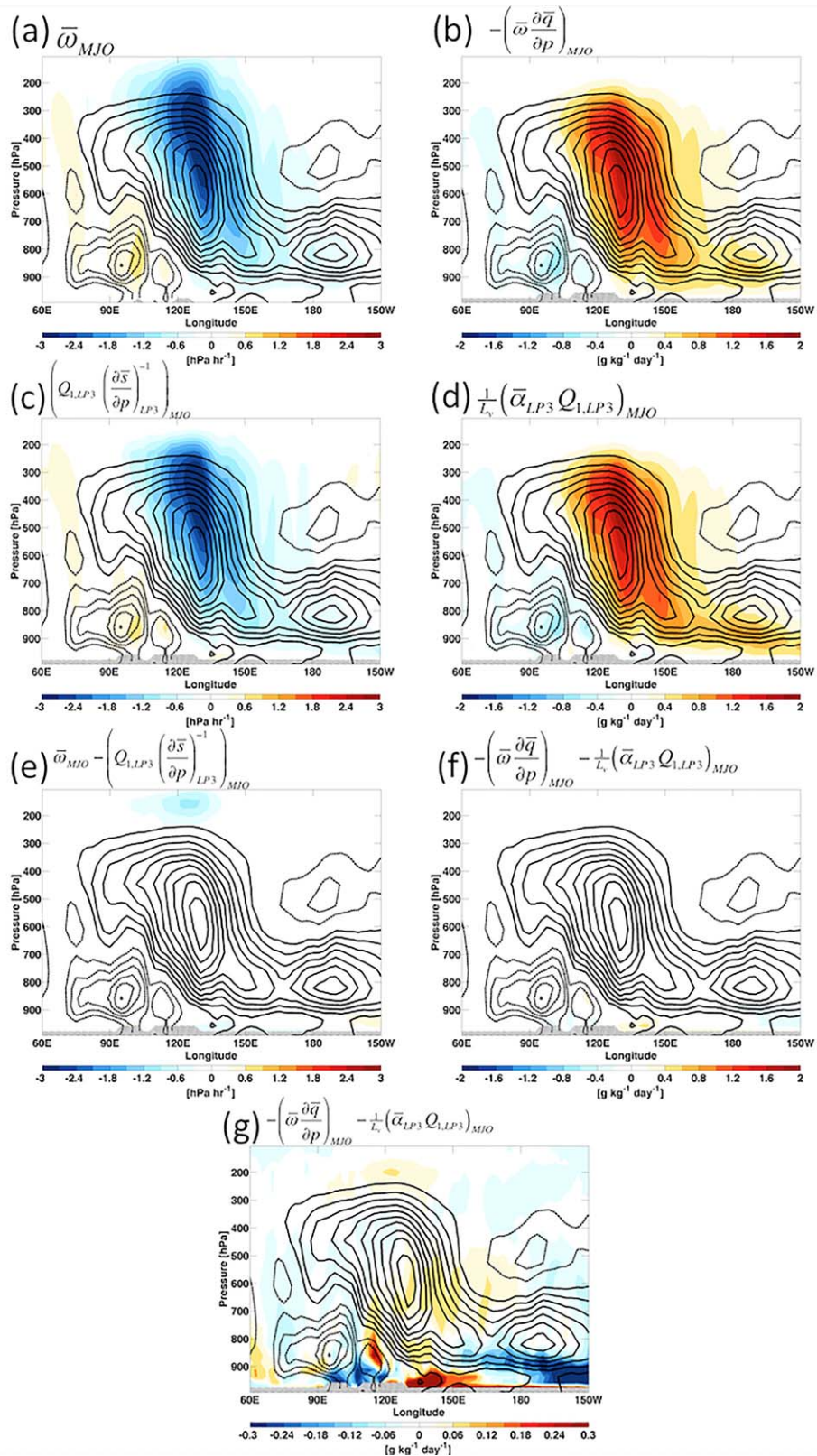
(A1)

where

Figure A1. As in Figure 11, except the color shading indicates the anomalous (a) large-scale vertical velocity and (b) vertical moisture advection in the $4\times CO_2$ simulation, the anomalous (c) large-scale vertical velocity and (d) vertical moisture advection diagnosed using weak temperature gradient balance assumptions, and the difference between the actual and diagnosed (e) large-scale vertical velocity and (f, g) vertical moisture advection. The subscripts LP3 and MJO indicate application of 3 day low-pass and 20–100 day band-pass filtering, respectively. Please note the color scale of Figure A1g differs from that of Figures A1b, A1d, and A1f.
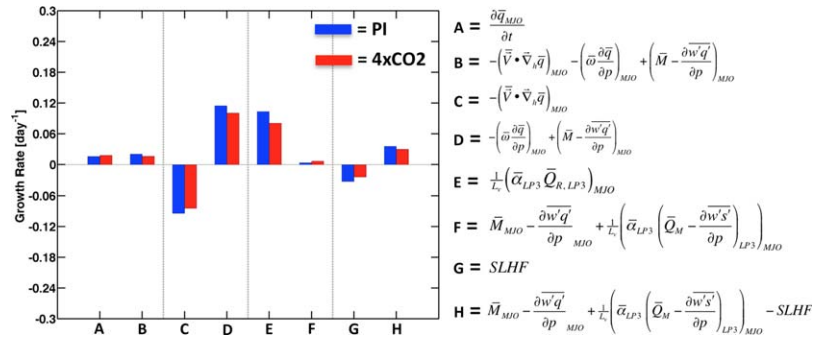
Figure A2. As in Figure 13, except expanded to include additional terms. The subscripts LP3 and MJO indicate application of 3 day low-pass and 20–100 day band-pass filtering, respectively. Terms E, F, and H were vertically integrated from 850 to 100 hPa, as they depend on the weak temperature gradient approximation.
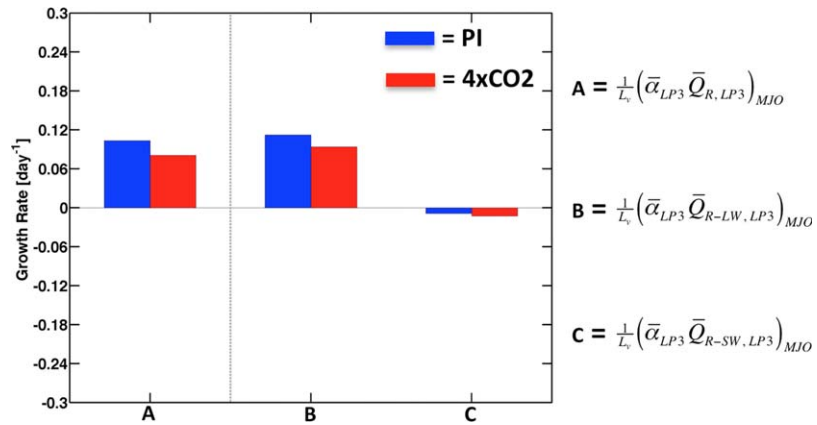

Figure A3. As in Figure 13, except for various radiative heating terms. The subscripts LP3 and MJO indicate application of 3 day low-pass and 20–100 day band-pass filtering, respectively. Each term was vertically integrated from 850 to 100 hPa, as they depend on the weak temperature gradient approximation.
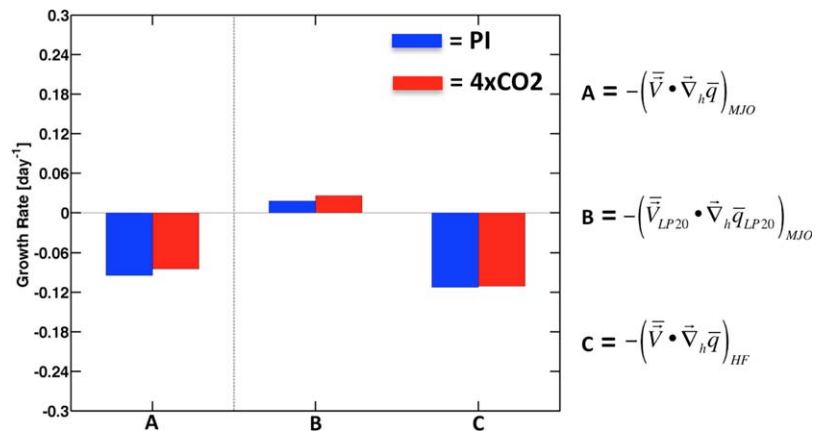

Figure A4. As in Figure 13, except for various horizontal advective terms. The subscripts LP20 and MJO indicate application of 20 day low-pass and 20–100 day band-pass filtering, respectively. The subscript HF indicates terms related to higher-frequency variability, calculated following equation (A2).
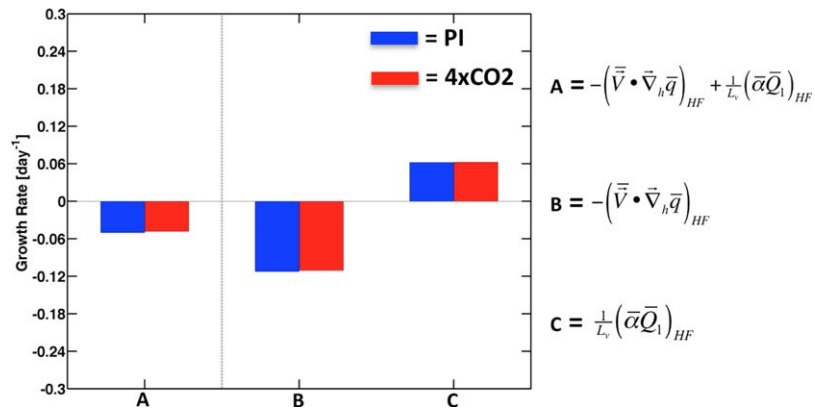
Figure A5. As in Figure 13, except for terms related to higher-frequency convective variability. The subscript HF indicates terms related to higher-frequency variability, calculated following equations (A2) and (A4). Term C was vertically integrated from 850 to 100 hPa, as it depends on the weak temperature gradient approximation.

$$\left(\mathbf{V}_h \cdot \nabla \bar{q} \right)_{HF} = \left(\mathbf{V}_{h,LP20} \cdot \nabla \bar{q}_{HP20} \right)_{MJO} + \left(\mathbf{V}_{h,HP20} \cdot \nabla \bar{q}_{LP20} \right)_{MJO} + \left(\mathbf{V}_{h,HP20} \cdot \nabla \bar{q}_{HP20} \right)_{MJO}, \tag{A2}$$

and the subscript $_{HP20}$ indicates the application of 20 day high-pass filtering. Similarly, using WTG balance, large-scale vertical moisture advection can be decomposed as

$$-\left(\bar{\omega} \frac{\partial \bar{q}}{\partial p} \right)_{MJO} = \frac{1}{L_v} \left(\left(\bar{\alpha}_{LP20} Q_{1,LP20} \right)_{MJO} + \left(\bar{\alpha} Q_1 \right)_{HF} \right), \tag{A3}$$

where

$$\left(\bar{\alpha} Q_1 \right)_{HF} = \left(\bar{\alpha}_{LP20} Q_{1,BP3-20} \right)_{MJO} + \left(\bar{\alpha}_{BP3-20} Q_{1,LP20} \right)_{MJO} + \left(\bar{\alpha}_{BP3-20} Q_{1,BP3-20} \right)_{MJO}, \tag{A4}$$

and the subscript $_{BP3-20}$ indicates the application of $3-20$ day band-pass filtering. The first term on the right-hand side of equations (A1) and (A3) result from slowly varying fields, while the second term on the right-hand side of both equations results from the presence of higher-frequency variability. These terms will be referred to as the horizontal advection and large-scale vertical moisture advection resulting from slowly varying fields and higher-frequency variability, respectively. Figure A4 shows total horizontal advection (term A) decomposed into contributions by slowly varying fields (term b) and higher-frequency variability (term C), respectively. In both simulations, horizontal advective damping (term A) results from the modulation of higher-frequency variability on intraseasonal timescales (term C), and the efficacy of this damping of moisture variance shows no change from the PI to $4\times CO_2$ simulation. As discussed in *Wolding et al.* [2016], modulation of higher-frequency convective variability also contributes to destabilization by large-scale vertical moisture advection, offsetting some of the horizontal advective damping effect. Figure A5 shows the total effect of higher-frequency convective variability, broken down into contributions from horizontal advection (term B) and large-scale vertical moisture advection (term C). Almost no change occurs in the effect of higher-frequency variability between the PI and $4\times CO_2$ simulations. These results further support the conclusion that no large changes occur in the balance of processes acting to destabilize the MJO.

References

Adames, Á. F., and D. Kim (2016), The MJO as a dispersive, convectively coupled moisture wave: Theory and observations, *J. Atmos. Sci.*, *73*(3), 913–941.

Arnold, N. P., and D. A. Randall (2015), Global-scale convective aggregation: Implications for the Madden-Julian oscillation, *J. Adv. Model. Earth Syst.*, *7*, 1499–1518, doi:10.1002/2015MS000498.

Arnold, N. P., Z. Kuang, and E. Tziperman (2013), Enhanced MJO-like variability at high SST, *J. Clim.*, *26*(3), 988–1001.

Arnold, N. P., M. Branson, Z. Kuang, D. A. Randall, and E. Tziperman (2015), MJO intensification with warming in the superparameterized CESM, *J. Clim.*, *28*(7), 2706–2724.

Bjerknes, J. (1966), A possible response of the atmospheric Hadley circulation to equatorial anomalies of ocean temperature, *Tellus*, *18*(4), 820–829.

Bony, S., B. Stevens, D. Coppin, T. Becker, K. A. Reed, A. Voigt, and B. Medeiros (2016), Thermodynamic control of anvil cloud amount, *Proc. Natl. Acad. Sci. U. S. A.*, *113*, 8927–8932.

Bretherton, C. S., M. E. Peters, and L. E. Back (2004), Relationships between water vapor path and precipitation over the tropical oceans, *J. Clim.*, *17*(7), 1517–1528.

Caballero, R., and M. Huber (2010), Spontaneous transition to superrotation in warm climates simulated by CAM3, *Geophys. Res. Lett.*, *37*, L11701, doi:10.1029/2010GL043468.

Carlson, H., and R. Caballero (2016), Enhanced MJO and transition to superrotation in warm climates, *J. Adv. Model. Earth Syst.*, *8*, 304–318, doi:10.1002/2015MS000615.

Carvalho, L. M., C. Jones, and T. Ambrizzi (2005), Opposite phases of the Antarctic oscillation and relationships with intraseasonal to inter-annual activity in the tropics during the austral summer, *J. Clim.*, *18*(5), 702–718.

Cassou, C. (2008), Intraseasonal interaction between the Madden–Julian oscillation and the north Atlantic oscillation, *Nature*, *455*(7212), 523–527.

Chikira, M. (2014), Eastward-propagating intraseasonal oscillation represented by Chikira–Sugiyama cumulus parameterization. Part II: Understanding moisture variation under weak temperature gradient balance, *J. Atmos. Sci.*, *71*(2), 615–639, doi:10.1175/JAS-D-13-038.1.

Fuchs, Z., and D. J. Raymond (2005), Large-scale modes in a rotating atmosphere with radiative-convective instability and WISHE, *J. Atmos. Sci.*, *62*(11), 4084–4094.

Grabowski, W. W. (2001), Coupling cloud processes with the large-scale dynamics using the cloud-resolving convection parameterization (CRCP), *J. Atmos. Sci.*, *58*(9), 978–997.

Hall, J. D., A. J. Matthews, and D. J. Karoly (2001), The modulation of tropical cyclone activity in the Australian region by the Madden-Julian oscillation, *Mon. Weather Rev.*, *129*(12), 2970–2982.

Hamill, T. M., and G. N. Kiladis (2014), Skill of the MJO and northern hemisphere blocking in GEFS medium-range reforecasts, *Mon. Weather Rev.*, *142*(2), 868–885.

Hand, E. (2015), The storm king, *Science*, *350*(6256), 22–25.

Held, I. M., and B. J. Soden (2006), Robust responses of the hydrological cycle to global warming, *J. Clim.*, *19*(21), 5686–5699.

Henderson, S. A., E. D. Maloney, and E. A. Barnes (2016), The influence of the Madden-Julian oscillation on northern hemisphere winter blocking, *J. Clim.*, in press.

Hoskins, B. J., and D. J. Karoly (1981), The steady linear response of a spherical atmosphere to thermal and orographic forcing, *J. Atmos. Sci.*, *38*(6), 1179–1196.

Hoskins, B. J., and T. Ambrizzi (1993), Rossby wave propagation on a realistic longitudinally varying flow, *J. Atmos. Sci.*, *50*(12), 1661–1671.

Hurrell, J. W., et al. (2013), The community earth system model: A framework for collaborative research, *Bull. Am. Meteorol. Soc.*, *94*(9), 1339–1360.

Janiga, M. A., and C. Zhang (2016), MJO moisture budget during dynamo in a cloud-resolving model, *J. Atmos. Sci.*, *73*(6), 2257–2278.

Jin, F., and B. J. Hoskins (1995), The direct response to tropical heating in a baroclinic atmosphere, *J. Atmos. Sci.*, *52*(3), 307–319.

Johnson, N. C., and S. B. Feldstein (2010), The continuum of north Pacific sea level pressure patterns: Intraseasonal, interannual, and inter-decadal variability, *J. Clim.*, *23*(4), 851–867.

Jones, C., and L. M. Carvalho (2006), Changes in the activity of the Madden-Julian oscillation during 1958-2004, *J. Clim.*, *19*(24), 6353–6370.

Khairoutdinov, M. F., and D. A. Randall (2003), Cloud resolving modeling of the arm summer 1997 IOP: Model formulation, results, uncertainties, and sensitivities, *J. Atmos. Sci.*, *60*(4), 607–625.

Kiladis, G. N., J. Dias, K. H. Straub, M. C. Wheeler, S. N. Tulich, K. Kikuchi, K. M. Weickmann, and M. J. Ventrice (2014), A comparison of OLR and circulation-based indices for tracking the MJO, *Mon. Weather Rev.*, *142*(5), 1697–1715.

Kim, D., A. H. Sobel, and I.-S. Kang (2011), A mechanism denial study on the Madden-Julian oscillation, *J. Adv. Model. Earth Syst.*, *3*, M12007, doi:10.1029/2011MS000081.

Knutson, T. R., and S. Manabe (1995), Time-mean response over the tropical Pacific to increased CO_2 in a coupled ocean-atmosphere model, *J. Clim.*, *8*(9), 2181–2199.

Lau, W. K., and D. Waliser (Eds.) (2012), Predictability and forecasting, in *Intraseasonal Variability in the Atmosphere-Ocean Climate System*, Springer, Chichester, U. K.

Lau, W. K., D. E. Waliser, and P. E. Roundy (2012), Tropical–extratropical interactions, in *Intraseasonal Variability in the Atmosphere-Ocean Climate System*, pp. 497–512, Springer, Chichester, U. K.

Lee, S. (1999), Why are the climatological zonal winds easterly in the equatorial upper troposphere?, *J. Atmos. Sci.*, *56*(10), 1353–1363.

L'Heureux, M. L., and R. W. Higgins (2008), Boreal winter links between the Madden-Julian oscillation and the arctic oscillation, *J. Clim.*, *21*(12), 3040–3050.

Lin, H., G. Brunet, and J. Derome (2009), An observed connection between the north Atlantic oscillation and the Madden-Julian oscillation, *J. Clim.*, *22*(2), 364–380.

Madden, R. A., and P. R. Julian (1971), Detection of a 40-50 day oscillation in the zonal wind in the tropical Pacific, *J. Atmos. Sci.*, *28*(5), 702–708.

Madden, R. A., and P. R. Julian (1972), Description of global-scale circulation cells in the tropics with a 40-50 day period, *J. Atmos. Sci.*, *29*(6), 1109–1123.

Maloney, E. D., and D. L. Hartmann (2000a), Modulation of eastern north Pacific hurricanes by the Madden-Julian oscillation, *J. Clim.*, *13*(9), 1451–1460.

Maloney, E. D., and D. L. Hartmann (2000b), Modulation of hurricane activity in the gulf of Mexico by the Madden-Julian oscillation, *Science*, *287*(5460), 2002–2004.

Maloney, E. D., and S.-P. Xie (2013), Sensitivity of tropical intraseasonal variability to the pattern of climate warming, *J. Adv. Model. Earth Syst.*, *5*(1), 32–47.

McPhaden, M. J. (1999), Genesis and evolution of the 1997-98 el Niño, *Science*, *283*(5404), 950–954.

Mori, M., and M. Watanabe (2008), The growth and triggering mechanisms of the PNA: A MJO-PNA coherence, *J. Meteorol. Soc. Jpn.*, *86*(1), 213–236.

Mundhenk, B. D., E. A. Barnes, and E. D. Maloney (2016), All-season climatology and variability of atmospheric river frequencies over the north Pacific, *J. Clim.*, in press.

Neelin, J. D., O. Peters, and K. Hales (2009), The transition to strong convection, *J. Atmos. Sci.*, *66*(8), 2367–2384.

North, G. R., T. L. Bell, R. F. Cahalan, and F. J. Moeng (1982), Sampling errors in the estimation of empirical orthogonal functions, *Mon. Weather Rev.*, *110*(7), 699–706.

Oliver, E. C., and K. R. Thompson (2012), A reconstruction of Madden-Julian oscillation variability from 1905 to 2008, *J. Clim.*, *25*(6), 1996–2019.

Peters, O., and J. D. Neelin (2006), Critical phenomena in atmospheric precipitation, *Nat. Phys.*, *2*(6), 393–396.

Pritchard, M. S., and C. S. Bretherton (2014), Causal evidence that rotational moisture advection is critical to the superparameterized Madden–Julian oscillation, *J. Atmos. Sci.*, *71*(2), 800–815.

Pritchard, M. S., and D. Yang (2016), Response of the superparameterized Madden-Julian oscillation to extreme climate and basic state variation challenges a moisture mode view, *J. Clim.*, in press

Randall, D., M. Khairoutdinov, A. Arakawa, and W. Grabowski (2003), Breaking the cloud parameterization deadlock, *Bull. Am. Meteorol. Soc.*, *84*(11), 1547–1564.

Raymond, D. J. (2001), A new model of the Madden-Julian oscillation, *J. Atmos. Sci.*, *58*(18), 2807–2819.

Raymond, D. J., and Ž. Fuchs (2009), Moisture modes and the Madden-Julian oscillation, *J. Clim.*, *22*(11), 3031–3046.

Riley Dellaripa, E. M., and E. D. Maloney (2015), Analysis of MJO wind-flux feedbacks in the Indian ocean using RAMA buoy observations, *J. Meteorol. Soc. Jpn.*, *93*, 1–20.

Roundy, P. E., K. MacRitchie, J. Asuma, and T. Melino (2010), Modulation of the global atmospheric circulation by combined activity in the Madden-Julian oscillation and the el Niño-southern oscillation during boreal winter, *J. Clim.*, *23*(15), 4045–4059.

Sahany, S., J. D. Neelin, K. Hales, and R. B. Neale (2012), Temperature-moisture dependence of the deep convective transition as a constraint on entrainment in climate models, *J. Atmos. Sci.*, *69*(4), 1340–1358.

Sardeshmukh, P. D., and B. J. Hoskins (1988), The generation of global rotational flow by steady idealized tropical divergence, *J. Atmos. Sci.*, *45*(7), 1228–1251.

Schubert, J. J., B. Stevens, and T. Crueger (2013), Madden-Julian oscillation as simulated by the MPI earth system model: Over the last and into the next millennium, *J. Adv. Model. Earth Syst.*, *5*(1), 71–84.

Shinoda, T., H. H. Hendon, and J. Glick (1998), Intraseasonal variability of surface fluxes and sea surface temperature in the tropical western Pacific and Indian oceans, *J. Clim.*, *11*(7), 1685–1702.

Slade, S. A., and E. D. Maloney (2013), An intraseasonal prediction model of Atlantic and east Pacific tropical cyclone genesis, *Mon. Weather Rev.*, *141*(6), 1925–1942.

Slingo, J., D. Rowell, K. Sperber, and F. Nortley (1999), On the predictability of the interannual behaviour of the Madden-Julian oscillation and its relationship with el Niño, *Q. J. R. Meteorol. Soc.*, *125*(554), 583–609.

Sobel, A., and E. Maloney (2012), An idealized semi-empirical framework for modeling the Madden-Julian oscillation, *J. Atmos. Sci.*, *69*(5), 1691–1705.

Sobel, A. H., J. Nilsson, and L. M. Polvani (2001), The weak temperature gradient approximation and balanced tropical moisture waves, *J. Atmos. Sci.*, *58*(23), 3650–3665.

Takayabu, Y. N., T. Iguchi, M. Kachi, A. Shibata, and H. Kanzawa (1999), Abrupt termination of the 1997–98 el Niño in response to a Madden–Julian oscillation, *Nature*, *402*(6759), 279–282.

Thompson, D. B., and P. E. Roundy (2013), The relationship between the Madden-Julian oscillation and us violent tornado outbreaks in the spring, *Mon. Weather Rev.*, *141*(6), 2087–2095.

Trenberth, K. E., G. W. Branstator, D. Karoly, A. Kumar, N.-C. Lau, and C. Ropelewski (1998), Progress during toga in understanding and modeling global teleconnections associated with tropical sea surface temperatures, *J. Geophys. Res.*, *103*(C7), 14,291–14,324.

Vecchi, G. A., and N. A. Bond (2004), The Madden-Julian oscillation (MJO) and northern high latitude wintertime surface air temperatures, *Geophys. Res. Lett.*, *31*, L04104, doi:10.1029/2003GL018645.

Watanabe, M., and M. Kimoto (2000), Atmosphere-ocean thermal coupling in the north Atlantic: A positive feedback, *Q. J. R. Meteorol. Soc.*, *126*(570), 3343–3369.

Wheeler, M. C., and H. H. Hendon (2004), An all-season real-time multivariate MJO index: Development of an index for monitoring and prediction, *Mon. Weather Rev.*, *132*(8), 1917–1932.

Wolding, B. O., and E. D. Maloney (2015), Objective diagnostics and the Madden–Julian oscillation. Part II: Application to moist static energy and moisture budgets, *J. Clim.*, *28*(19), 7786–7808.

Wolding, B. O., E. D. Maloney, and M. Branson (2016), Vertically resolved weak temperature gradient analysis of the Madden-Julian oscillation in SP-CESM, *J. Adv. Model. Earth Syst.*, *8*, doi:10.1002/2016MS000724.

Yanai, M., S. Esbensen, and J.-H. Chu (1973), Determination of bulk properties of tropical cloud clusters from large-scale heat and moisture budgets, *J. Atmos. Sci.*, *30*(4), 611–627.

Zhang, C. (2005), Madden-Julian oscillation, *Rev. Geophys.*, *43*, RG2003, doi:10.1029/2004RG000158.

Zhang, C. (2013), Madden-Julian oscillation: Bridging weather and climate, *Bull. Am. Meteorol. Soc.*, *94*(12), 1849–1870.

Zhou, S., and A. J. Miller (2005), The interaction of the Madden-Julian oscillation and the arctic oscillation, *J. Clim.*, *18*(1), 143–159.

Zhou, S., M. L'Heureux, S. Weaver, and A. Kumar (2012), A composite study of the MJO influence on the surface air temperature and precipitation over the continental united states, *Clim. Dyn.*, *38*(7–8), 1459–1471.